

A High-Order Shifted Interface Method for Lagrangian Shock Hydrodynamics

Nabil M. Atallah^{a,b}, Ketan Mittal^b, Guglielmo Scovazzi^a, Vladimir Z. Tomov^{b,*}

^aDepartment of Civil and Environmental Engineering, Duke University, Durham, North Carolina 27708, USA

^bLawrence Livermore National Laboratory, Livermore (CA), USA

Abstract

We present a new method for two-material Lagrangian hydrodynamics, which combines the Shifted Interface Method (SIM) with a high-order Finite Element Method. Our approach relies on an exact (or sharp) material interface representation, that is, it uses the precise location of the material interface. The interface is represented by the zero level-set of a continuous high-order finite element function that moves with the material velocity. This strategy allows to evolve curved material interfaces inside curved elements. By reformulating the original interface problem over a surrogate (approximate) interface, located in proximity of the true interface, the SIM avoids cut cells and the associated problematic issues regarding implementation, numerical stability, and matrix conditioning. Accuracy is maintained by modifying the original interface conditions using Taylor expansions. We demonstrate the performance of the proposed algorithms on established numerical benchmarks in one, two and three dimensions.

Keywords: Lagrangian hydrodynamics; material interfaces; embedded methods; Shifted Boundary Method; high-order finite elements; curved meshes.

1. Introduction

Lagrangian methods for compressible multi-material shock hydrodynamics [1, 10, 14, 24, 25, 28, 32, 38–40] are characterized by a computational mesh that moves with the material velocity. A key advantage of these methods is that they do not produce any numerical dissipation around material interfaces, when these are aligned with the element boundaries of the moving mesh. The deforming mesh, however, inevitably deteriorates in quality, which can lead to small time steps or simulation breakdowns. This motivates the use of Arbitrary Lagrangian/Eulerian (ALE) methods [3, 7, 11, 16, 18, 29, 33, 46], where the solution fields are periodically projected on a better mesh. The new mesh generally loses the alignment with the material interfaces, producing cut elements that contain multiple materials. The focus of this paper is how to evolve such mixed elements while maintaining the key advantage of Lagrangian methods, that is, no dissipation around material interfaces.

Methods that process mixed elements, or *closure models* [20], can be classified into two major categories. The first treats a mixed element as a whole, without considering an explicit sub-element interface location [30]. Material concentrations are represented by volume fractions, and all material-specific quantities are evolved by introducing an equilibration mechanism for certain quantity, e.g., pressure [34, 35, 48], pressure and viscosity as in Section 3.1 of [20], velocity increments as in Section 4.4 of [48], pressure and heat changes [13]. The second approach makes use of material interface reconstruction within the mixed elements [41, 42, 49]. Most methods in this category employ of acoustic Riemann solvers in order to predict quantities like interface velocity, material volume changes, and pressure [6, 19].

*Corresponding author: Vladimir Tomov

Email addresses: atallah1@llnl.gov (Nabil M. Atallah), mittal3@llnl.gov (Ketan Mittal), guglielmo.scovazzi@duke.edu (Guglielmo Scovazzi), tomov2@llnl.gov (Vladimir Z. Tomov)

High-order Finite Element Methods (FEMs) for Lagrangian hydrodynamics on curved grids have recently gained popularity as they allow both high physics resolution [3, 14, 17], and efficient computational performance on the latest computer architectures [21, 45]. The initial approach to evolve mixed elements in these method was developed in [15], utilizing the first of the above closure approaches, mainly because reconstructing curved interfaces within curved elements was not an existing technology at the time. While results have been good in most problems, the diffuse-interface nature of the method tends to propagate small volume fractions away from the contact regions, especially in simulations involving many ALE steps over large material displacements [3, 15]. Diffuse-interface methods that reduce the size of the diffused regions have been developed [34, 35, 47], but the interface is still approximate and some amount of diffusion is still present.

Recently, the Shifted Interface Method (SIM) [23] was proposed, as an alternative FEM for interface problems. By reformulating the original interface problem over a surrogate (approximate) interface, located in proximity of the true interface, the SIM avoids cut cells and the associated problematic issues regarding implementation, numerical stability, and matrix conditioning. Accuracy is maintained by modifying the original interface conditions using Taylor expansions.

The SIM was derived from the Shifted Boundary Method (SBM) [26, 27], which uses the same strategy for the approximation of boundary conditions. The SBM was applied to simple hyperbolic systems of conservations laws, such as the equations of acoustics and shallow-water flows [43]. Some preliminary developments in combining the SBM with high-order discretizations were also made in [5], for the Poisson and Stokes problems.

The SIM approach preserves all favorable properties of high-order FE discretizations (optimal convergence, generality with respect to space dimension, element type, and FE polynomial order), while allowing a notion of exact interface representation without any explicit geometric operations. The generality of the SIM makes it an obvious approach for evolving exact curved interfaces in the framework of [14], which is the goal of this work.

In this paper we transform the single-material high-order FEM of [14] into a two-material Lagrangian method that evolves mixed elements through the SIM. The material interface is represented by the zero level set (LS) of a continuous high-order finite element function η that moves with the material velocity, i.e., η is constant in time in the Lagrangian frame. The zero LS of η , which from now on will also be called the *true interface*, is used to define a *surrogate interface* where the interface conditions will be applied; these surrogates are a subset of the mesh faces. Distance vectors between the surrogate and true interface (the zero LS of η) are computed by a FE distance solver. The interface conditions are imposed weakly by defining face integrals over the surrogate faces. Taylor expansions along the distance vectors are used to compensate for the difference in location between the true and surrogate interface conditions. The above procedure allows the method to have a notion of exact (or sharp) interface location, that is, it uses a precise interface location in the material-related calculations. The interface evolution does not involve any geometric operations and is general with respect to dimension, mesh curvature, and FE discretization order.

The rest of the paper is organized as follows. Section 2 reviews the equations of Lagrangian hydrodynamics, their FE discretization in [14], and the targeted interface conditions. Section 3 introduces the general concepts of the SIM, starting in a broader context, and then moving to the specifics of two-material shock hydrodynamics. Then Section 4 gives the FE discretization details in the case of interest, derives the SIM formulation, and discusses its conservation properties. Numerical tests are presented in Section 5. Finally Section 6 provides some conclusions and future work.

2. General equations and finite element discretization

This work builds on an existing single-material Lagrangian method [14]. In this section, we briefly go over the underlying equations and their discretization in the finite element framework; the complete description can be found in [14].

2.1. Governing equations

The classical equations of Lagrangian shock hydrodynamics govern the rate of change in position \mathbf{x} , velocity \mathbf{v} , and specific internal energy e of a compressible body of fluid as it deforms. Let Ω_0 and Ω be open sets in \mathbb{R}^d

where d is the number of spatial dimensions. The motion map

$$\varphi : \Omega_0 \rightarrow \Omega, \quad \varphi(\mathbf{x}_0, t) = \mathbf{x}, \quad \forall \mathbf{x}_0 \in \Omega_0, \forall t \geq 0, \quad (1)$$

maps the material coordinate \mathbf{x}_0 , representing the initial position of an infinitesimal material particle of the body, to \mathbf{x} , the position of the same particle in the current configuration, see Figure 1. Using the deformation gradient $\mathbf{F}(\mathbf{x}, t) = \nabla_{\mathbf{x}_0} \varphi(\mathbf{x}, t)$ and its corresponding Jacobian $J(\mathbf{x}, t) = \det(\mathbf{F})$, the material density ρ is evolved pointwise by:

$$\rho(\mathbf{x}, t) = \frac{\rho_0(\mathbf{x}_0)}{J(\mathbf{x}, t)}. \quad (2)$$

The material velocity \mathbf{v} and position \mathbf{x} are represented by finite element functions in the space $\mathcal{V} \subset [H^1(\Omega)]^d$. We will indicate by \mathbf{w} the kinematic (vector) test function in \mathcal{V} . The specific internal energy e is discretized in $\mathcal{E} \subset L_2(\Omega)$, with a corresponding (scalar) test function ϕ . Throughout this manuscript, we refer to the pairs of spaces $(Q_m)^d - \hat{Q}_{m-1}$, by which $(Q_m)^d = \mathcal{V}$ is the Cartesian product of the space of continuous finite elements on quadrilateral or hexahedral meshes of degree m , and $\hat{Q}_{m-1} = \mathcal{E}$ is the companion space of discontinuous finite elements of order one less than the kinematic space. The semi-discrete system is:

$$\frac{d\mathbf{x}}{dt} = \mathbf{v}, \quad (3a)$$

$$\int_{\Omega(t)} \mathbf{w} \cdot \left(\rho \frac{d\mathbf{v}}{dt} \right) = \int_{\Omega(t)} \nabla \mathbf{w} : (p\mathbf{I} - \sigma_a), \quad (3b)$$

$$\int_{\Omega(t)} \phi \rho \frac{de}{dt} = \int_{\Omega(t)} \phi (-p \nabla \cdot \mathbf{v} + \sigma_a : \nabla \mathbf{v}), \quad (3c)$$

where p is the thermodynamic pressure, computed from an equation of state of the type $p = \mathcal{P}(\rho, e)$, and σ_a is the artificial viscosity stress tensor, which provides numerical stability in the presence of shocks, see Section 6 in [14]. Note also that d/dt indicates the total material derivative (or Lagrangian derivative), i.e., for some field ϑ , we have $d\vartheta/dt = \partial\vartheta/\partial t + \mathbf{v} \cdot \nabla\vartheta$.

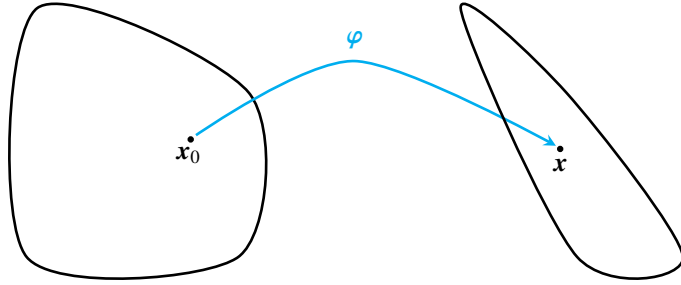


Figure 1: Sketch of the Lagrangian map φ .

Interface conditions. When multiple materials are present in the domain Ω , the principles of mass and momentum conservation imply specific conditions at the interfaces separating the materials. For the sake of simplicity and without loss of generality, consider the case of two materials and an interface separating them. Let Ω be the physical domain of the problem, a bounded and connected open region in \mathbb{R}^n ($n = 2$ or 3). Let $\Gamma := \partial\Omega$ be the Lipschitz boundary of Ω , composed as the union of C^2 curves (in two dimensions) or surfaces (in three dimensions) that intersect at a finite number of vertices or edges. We assume that Ω is partitioned by an interface Γ_I into two non-overlapping domains satisfying $\Omega = \Omega_1 \cup \Omega_2 \cup \Gamma_I$, as shown in Figure 2. Here $\Omega_1 \cup \Omega_2 \neq \emptyset$ and $\Gamma_I = \text{clos}(\Omega_1) \cap \text{clos}(\Omega_2)$ defines the internal interface (also assumed Lipschitz) between Ω_1 and Ω_2 . Then the

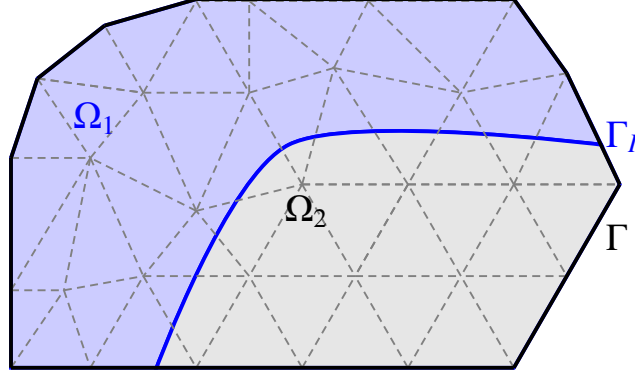


Figure 2: The true domain Ω , with boundary $\Gamma = \partial\Omega$, and the internal interface Γ_I , which decomposes Ω as $\Omega = \Omega_1 \cup \Omega_2 \cup \Gamma_I$.

system of equations (3a) would hold on $\Omega = \Omega_1 \cup \Omega_2$ with the following interface conditions on Γ_I :

$$[[p]] = 0, \quad (4a)$$

$$[[\mathbf{v}]] \cdot \mathbf{n}_1 = 0. \quad (4b)$$

Note that $[[p]] = (p_1 - p_2)\mathbf{n}_1$, $[[\mathbf{v}]] = \mathbf{v}^+ - \mathbf{v}^-$ indicate jumps in pressure and velocity, with \mathbf{n}_1 and \mathbf{n}_2 the outward-pointing normals to $\partial\Omega_1$ and $\partial\Omega_2$, respectively. It is also useful to define the average $\{\{\zeta\}\}_\gamma = \gamma \zeta_1 + (1 - \gamma) \zeta_2$ for $\gamma \in \{0, 1\}$.

Remark 1. We choose to enforce the pressure condition (4a) as this is common in most closure model approaches [6, 15, 34, 48]. Applications often require a more sophisticated condition on the normal component of the full stress tensor, including the artificial viscosity, namely,

$$[[-p\mathbf{I} + \boldsymbol{\sigma}_a)\mathbf{n}_1]] = 0.$$

In principle the shifted approach can be used to enforce such condition, and we will consider this in the future. The present work focuses on the simpler pressure condition (4a).

2.2. Integration and infinite dimensional function spaces

In the sequel, $(v, w)_\omega = \int_\omega v w$ denotes the L^2 inner product on a subset $\omega \subset \Omega$ and $\langle v, w \rangle_\zeta = \int_\zeta v w$ denotes the L^2 inner product on a subset ζ of one of the boundaries or interfaces present in Ω . Throughout the paper, we will use the Sobolev spaces $H^m(\Omega) = W^{m,2}(\Omega)$ of index of regularity $m \geq 0$ and index of summability 2, equipped with the (scaled) norm

$$\|v\|_{H^m(\Omega)} = \left(\|v\|_{L^2(\Omega)}^2 + \sum_{k=1}^m \|l(\Omega)^k \mathbf{D}^k v\|_{L^2(\Omega)}^2 \right)^{1/2}, \quad (5)$$

where \mathbf{D}^k is the k th-order spatial derivative operator and $l(A) = (\text{meas}(A))^{1/n_d}$ is a characteristic length of the domain A . Note that $H^0(\Omega) = L^2(\Omega)$. As usual, we use a simplified notation for norms and semi-norms, i.e., we set $\|v\|_{m;\Omega} = \|v\|_{H^m(\Omega)}$ and $|v|_{k;\Omega} = \|\mathbf{D}^k v\|_{0;\Omega} = \|\mathbf{D}^k v\|_{L^2(\Omega)}$.

3. A general introduction to the Shifted Interface Method

3.1. The triangulation \mathcal{T}^h of Ω

Let \mathcal{T}^h be a family of admissible and shape-regular triangulations of Ω . In what follows, we will make the specific assumption that the triangulation \mathcal{T}^h is *fitted* to the boundary Γ of Ω . The set of all edges (in two dimensions) or faces (in three dimensions) of the triangulation \mathcal{T}^h is indicated as \mathcal{E} . We indicate by h_T the diameter of an element $T \in \mathcal{T}^h$ and by h the piecewise constant function in Ω such that $h_T = h_T$ for all $T \in \mathcal{T}^h$.

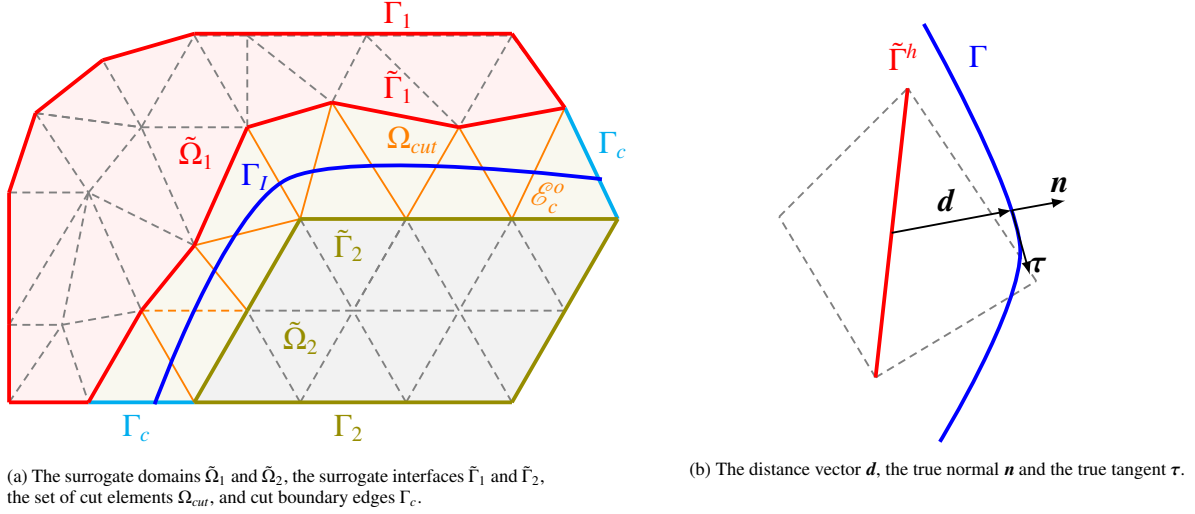


Figure 3: The surrogate domain, its boundary, and the distance vector d .

3.2. The true domain, the surrogate domain and maps

As shown in Figure 3a, consider a grid, fitted to the boundary $\Gamma = \partial\Omega$, but not to Γ_I . We can then define the triangulations $\tilde{\mathcal{T}}_1^h$ and $\tilde{\mathcal{T}}_2^h$ by selecting those elements that are *strictly* contained in the closure of Ω_1 and Ω_2 respectively, i.e.,

$$\tilde{\mathcal{T}}_i^h := \{T \in \mathcal{T}^h : T \subset \text{clos}(\Omega_i)\}, \quad (6)$$

where $i = 1$ or 2 . $\tilde{\mathcal{T}}_1^h$ and $\tilde{\mathcal{T}}_2^h$ then identify the surrogate domains $\tilde{\Omega}_1$ and $\tilde{\Omega}_2$ (the areas shaded in red and dark green in Figure 3a). Namely, for $i = 1$ or 2 ,

$$\tilde{\Omega}_i := \text{int} \left(\bigcup_{T \in \tilde{\mathcal{T}}_i^h} T \right) \subseteq \Omega_i. \quad (7)$$

Furthermore, the set of all edges (in two dimensions) or faces (in three dimensions) of the triangulation $\tilde{\mathcal{T}}_1^h$ and $\tilde{\mathcal{T}}_2^h$ is indicated as \mathcal{E}_1 and \mathcal{E}_2 , respectively. We also define the subset of elements that are cut by Γ_I , namely

$$\mathcal{T}_c^h := \{T \in \mathcal{T}^h : T \cap \Gamma_I \neq \emptyset\}, \quad (8)$$

and the corresponding *cut domain*

$$\Omega_c := \text{int} \left(\bigcup_{T \in \mathcal{T}_c^h} T \right). \quad (9)$$

We denote by

$$\Gamma_i := \tilde{\Omega}_i \cap \Gamma \quad (10)$$

the body-fitted faces and by

$$\tilde{\Gamma}_i := \Omega_c \cap \tilde{\Omega}_i \quad (11)$$

the surrogate faces. The set of all interior edges/faces of the triangulation $\tilde{\mathcal{T}}^h$, $\tilde{\mathcal{T}}_1^h$ and $\tilde{\mathcal{T}}_2^h$ is indicated by $\mathcal{E}^o = \mathcal{E} \setminus \Gamma$, $\mathcal{E}_1^o = \mathcal{E}_1 \setminus \Gamma_1$ and $\mathcal{E}_2^o = \mathcal{E}_2 \setminus \Gamma_2$, respectively. $\mathcal{E}_c^o = \{E \in \mathcal{E} \setminus \Gamma : E \cap \Gamma_I \neq \emptyset\}$ indicates the union of *interior* edges/faces (in two/three dimensions, resp.) that are cut by Γ_I (marked in orange in Figure 3a). Finally, we denote by

$$\Gamma_c := \partial\Omega_c \setminus (\tilde{\Gamma}_1 \cup \tilde{\Gamma}_2) \quad (12)$$

the subset of edges/faces on the boundary Γ of Ω that belong to elements in Ω_c (depicted in light blue, in Figure 3a).

3.3. Maps from the surrogate to the true interfaces

We now define the map

$$\tilde{\mathbf{M}}_i : \tilde{\Gamma}_i \rightarrow \Gamma, \quad \forall i \in \{1, 2\} \quad (13a)$$

$$\tilde{\mathbf{x}}_i \mapsto \mathbf{x}, \quad (13b)$$

which maps a point $\tilde{\mathbf{x}} \in \tilde{\Gamma}_i$ on the surrogate free surface to a point $\mathbf{x} \in \Gamma_I$ on the true free surface. More generally, $\tilde{\mathbf{M}}_i$ is a map between a surrogate and true boundaries in an immersed/embedded/unfitted domain computation, and can be built using the *closest-point projection* of points in $\tilde{\Gamma}_i$ onto Γ_I , as shown in Figure 3b. In particular, it will become very important to characterize the map $\tilde{\mathbf{M}}_i$ through a distance vector function

$$\mathbf{d}_{\tilde{\mathbf{M}}_i}(\tilde{\mathbf{x}}) = \mathbf{x} - \tilde{\mathbf{x}}_i = [\tilde{\mathbf{M}}_i - \mathbf{I}](\tilde{\mathbf{x}}). \quad (14)$$

As shown in Figure 3b, if the closest-point projection is used, the vector \mathbf{d} is aligned with \mathbf{n} . This case is typical when Γ_I is a smooth surface, while we refer to [4] for the case when edges/corners are present or when multiple boundary conditions are enforced on a smooth surface. Moreover, we will denote by $\tilde{\mathbf{n}}_i$ the unit outward-pointing normal to the surrogate faces $\tilde{\Gamma}_i$, to be distinguished from the outward-pointing normal \mathbf{n} to the true interface Γ_I .

Equivalently, we can find a map $\mathbf{M}_c : E \in \mathcal{E}_c^o \rightarrow \Gamma_I$, defined by means of the distance $\mathbf{d}_{\mathbf{M}_c} = \mathbf{x} - \mathbf{x}_c$, from a point on $\mathbf{x}_c \in \mathcal{E}_c^o$, to its closest point projection on the true interface, $\mathbf{x} \in \Gamma_I$. For the sake of simplicity and whenever there is no chance of confusion, the “tilde” and the subscript c will be omitted from the map symbols $\tilde{\mathbf{M}}$ and \mathbf{M}_c , and will simply write “ \mathbf{M} .” Similarly, we will omit the subscripts of $\mathbf{d}_{\tilde{\mathbf{M}}_i}$ and $\mathbf{d}_{\mathbf{M}_c}$, and write “ \mathbf{d} .”

Remark 1. In this work, the distance vector \mathbf{d} is defined by means of the zero level set of a distance function, which is always well defined if the interface Γ_I is Lipschitz. This approach is presented in full details in Section 3.5. We also point the reader to the recent analysis in [4], where the SBM and associated boundary maps are implemented for general domains with corners and edges. Most importantly, the methods that we are about to introduce do not depend on how \mathbf{M} is constructed.

3.4. General strategy for interface conditions

While the governing equations are discretized over Ω , the interface conditions (4a)-(4b) will be imposed on $\tilde{\Gamma}_i \cup \mathcal{E}_c^o$ rather than Γ_I . As such, the challenge is to appropriately impose interface conditions on $\tilde{\Gamma}_i \cup \mathcal{E}_c^o$ that would mimic (4a)-(4b). To this end, we resort to the m^{th} -order Taylor expansion of the variables of interest, centered at $\tilde{\Gamma}_i \cup \mathcal{E}_c^o$. This approach allows to *shift* the interface conditions from Γ_I to $\tilde{\Gamma}_i \cup \mathcal{E}_c^o$.

Starting with the interface condition involving the pressure, let us assume that p is sufficiently smooth so as to admit a m^{th} -order Taylor expansion pointwise, and let us denote by \mathcal{D}_d^k the k^{th} -order directional derivative in

the direction of \mathbf{d} , defined as $\mathcal{D}_d^k p = \sum_{\alpha \in \mathbb{N}^n, |\alpha|=k} \frac{k!}{\alpha!} \frac{\partial^k p}{\partial \mathbf{x}^\alpha} \mathbf{d}^\alpha$. Then, we can write

$$\llbracket p(\mathbf{x}) \rrbracket = \llbracket p(\tilde{\mathbf{x}} + \mathbf{d}(\tilde{\mathbf{x}})) \rrbracket = \llbracket p(\tilde{\mathbf{x}}) + \sum_{k=1}^{m-1} \frac{\mathcal{D}_d^k p(\tilde{\mathbf{x}})}{k!} + (R^m(p, \mathbf{d}))(\tilde{\mathbf{x}}) \rrbracket = 0, \quad (15)$$

where the remainder $R^m(p, \mathbf{d}) = o(\|\mathbf{d}\|^m)$ as $\|\mathbf{d}\| \rightarrow 0$. Now we introduce the operator

$$S_h^{m-1} p := p + \sum_{k=1}^{m-1} \frac{\mathcal{D}_{\mathbf{d}}^k p}{k!}, \quad (16)$$

Then the Taylor expansion can be used to enforce (4a) on $\tilde{\Gamma}_i \cup \mathcal{E}_c^o$ rather than Γ_I , as

$$\llbracket S_h^{m-1} p + R^{m-1}(p, \mathbf{d}) \rrbracket = 0, \quad (17)$$

which can be equivalently written as

$$\llbracket p \rrbracket = -\llbracket \sum_{k=1}^{m-1} \frac{\mathcal{D}_{\mathbf{d}}^k p}{k!} + R^m(p, \mathbf{d}) \rrbracket. \quad (18)$$

Neglecting the remainder $R^m(p, \mathbf{d})$, we obtain the final expression of the *shifted* interface condition on the pressure

$$\llbracket S_h^{m-1} p \rrbracket = \left(p_1 + \sum_{k=1}^{m-1} \frac{\mathcal{D}_{\mathbf{d}}^k p_1}{k!} - p_2 - \sum_{k=1}^{m-1} \frac{\mathcal{D}_{\mathbf{d}}^k p_2}{k!} \right) \mathbf{n}_1(\mathbf{M}(\tilde{\mathbf{x}})) = 0, \quad \text{on } \tilde{\Gamma}_i \cup \mathcal{E}_c^o, \quad (19)$$

which will be weakly enforced on the discretization p_h of p that will be introduced later. Similarly, for a vector field \mathbf{v} , we enforce

$$\llbracket S_h^m \mathbf{v} + \mathbf{R}^{m+1}(\mathbf{v}, \mathbf{d}) \rrbracket \cdot \mathbf{n}_1(\mathbf{M}(\tilde{\mathbf{x}})) = 0, \quad \text{on } \tilde{\Gamma}_i \cup \mathcal{E}_c^o \quad (20)$$

where $S_h^m \mathbf{v} := \mathbf{v} + \sum_{k=1}^m \frac{\mathcal{D}_{\mathbf{d}}^k \mathbf{v}}{k!}$ and $\mathbf{R}^{m+1}(\mathbf{v}, \mathbf{d})$ is the Taylor expansion remainder of \mathbf{v} on $\tilde{\Gamma}_i \cup \mathcal{E}_c^o$. Again, neglecting the the remainder $\mathbf{R}^{m+1}(\mathbf{v}, \mathbf{d})$, we obtain the *shifted* vector boundary condition

$$\llbracket S_h^m \mathbf{v} \rrbracket \cdot \mathbf{n}_1(\mathbf{M}(\tilde{\mathbf{x}})) = 0, \quad \text{on } \tilde{\Gamma}_i \cup \mathcal{E}_c^o. \quad (21)$$

which is equivalent to

$$\llbracket \mathbf{v} \rrbracket \cdot \mathbf{n}_1(\mathbf{M}(\tilde{\mathbf{x}})) = -\left(\llbracket \sum_{k=1}^m \frac{\mathcal{D}_{\mathbf{d}}^k \mathbf{v}}{k!} \rrbracket \right) \cdot \mathbf{n}_1(\mathbf{M}(\tilde{\mathbf{x}})), \quad \text{on } \tilde{\Gamma}_i \cup \mathcal{E}_c^o. \quad (22)$$

In what follows, whenever it does not cause confusion, we will simply write \mathbf{n}_1 in place of $\mathbf{n}_1(\mathbf{M}(\tilde{\mathbf{x}}))$.

3.5. Interface representation and distance computation

As we are interested in time-dependent problems, in which the material interface moves with the fluid velocity, the interface location must be represented by a dynamic discrete function. We utilize the standard Level-Set (LS) approach [44] where the interface is described by the zero LS of a finite element function η . Since the amount of deformation in time would be limited by the resolution of the kinematic FE space, it is natural to choose η in Q_m , i.e., the scalar version of the continuous FE space $\mathcal{V} = (Q_m)^d$ of the position \mathbf{x} and velocity \mathbf{v} . Once initialized, the LS function η is simply evolved by

$$\frac{d\eta}{dt} = 0, \quad (23)$$

which guarantees that the interface does not move into new elements and stays continuous throughout the Lagrangian simulation, while it follows the velocity curvature.

All shifted integrals require knowledge of the pointwise distance vector $\mathbf{d}(\mathbf{x})$ to the zero LS of η . There are many methods to compute such distances in the literature and we refer the reader to a recent summary given in [9]. In this work we make use of two distance computation methods. The first one is a simple renormalization

procedure given by

$$d(\mathbf{x}) = \frac{\eta(\mathbf{x})}{\sqrt{\eta(\mathbf{x})^2 + |\nabla\eta(\mathbf{x})|^2}}, \quad (24)$$

where $d(\mathbf{x}) \in Q_m$ is the signed scalar distance from \mathbf{x} to the zero LS of η (see Section 6 of [9]). This is a very fast pointwise computation which gives reasonable accuracy only in the vicinity of the zero level set. This outcome usually suffices for our purposes since all shifted computations primarily focus on the first band of elements surrounding the zero level set.

The second method to compute a FE distance function $d(\mathbf{x})$ utilizes the p-Laplacian distance computation (see Section 7 in [9]). That is, the magnitude $d(\mathbf{x}) \in Q_m$ of the distance vector $\mathbf{d} \in Q_m^d$ is the solution of:

$$\begin{aligned} \nabla \cdot (|\nabla d|^{p-2} \nabla d) &= -1 \text{ in } \Omega, \\ d &= 0 \text{ on } \partial\Omega, \quad 2 \leq p < \infty. \end{aligned} \quad (25)$$

This formulation computes the signed distance with respect to the boundary of any domain Ω , but the same approach can be customized for an arbitrary LS of a discrete function, by choosing appropriate finite element basis functions (see Section 3 in [37]). This approach is more expensive computationally, but offers improved accuracy.

In principle the distance function $d(\mathbf{x})$ must be updated after every Lagrangian time step through (24) or (25), as the mesh deformation at t^{n+1} deteriorates the signed distance property of d^n . In the case of the more expensive calculation (25), the update can be deferred by a few steps, assuming that the deterioration is not rapid. An alternative approach is to evolve directly the signed distance FE function $d(\mathbf{x})$ with an additional redistancing procedure, for example as in [8, 36].

4. The Weighted Shifted Interface Method

The Weighted Shifted Interface Method (WSIM) is inspired by the Weighted Shifted Boundary Method (WSBM), which was proposed in [12] for boundary value problems associated with the Navier-Stokes equations with free surfaces. The key idea in both methods is to weight the variational formulation by the volume fraction of the material(s), as a way to enhance the mass conservation properties of the overall algorithm. In what follows, we adapt the WSBM to the specific case of shock hydrodynamics interfaces, and in particular the high-order computational framework proposed in [14].

4.1. Finite Element spaces

For an element $T \in \mathcal{T}_h$, let the volume fraction, $\alpha_{i,T}$, for material $i \in \{1, 2\}$ be defined as

$$\alpha_{1,T}(t) = \frac{\int_{T(t)} H(\eta(\mathbf{x}, t))}{\text{meas}(T(t))}, \quad \alpha_{2,T}(t) = 1 - \alpha_{1,T}(t), \quad (26)$$

where H is the Heaviside step function. Clearly $\alpha_{i,T} \in [0, 1]$ and more precisely: $\alpha_{i,T} = 1$ if $T \subset \tilde{\Omega}_i$; $0 < \alpha_{i,T} < 1$ if $T \in \Omega_c$. We also construct the global function $\alpha_i(\mathbf{x}, t) \in \tilde{\Omega}_i \cup \Omega_c$ such that $\alpha_i|_T = \alpha_T$. Hence, $\alpha_i \in \mathcal{P}^0(\tilde{\mathcal{T}}_i^h \cup \mathcal{T}_c^h)$ where $\mathcal{P}^0(\tilde{\mathcal{T}}_i^h \cup \mathcal{T}_c^h)$ is the set of piecewise constant functions over $\tilde{\mathcal{T}}_i^h \cup \mathcal{T}_c^h$. Also note that (26) is time dependent due to the mesh motion. The numerator of (26) is computed approximately, by taking a large number of quadrature points in T that are either inside or outside of Ω_i ; more sophisticated integration methods can also be used to obtain better accuracy, for example [31].

We now define the following *weighted* velocity and pressure spaces:

$$\begin{aligned} \mathbf{V}_{\alpha_i}^h(\Omega, \mathcal{T}^h) &:= \left\{ \mathbf{v}_{\alpha_i}^h \in L_2(\Omega) : \mathbf{v}_{\alpha_i}^h = \alpha_i \mathbf{v}^h, \mathbf{v}^h \in H^1(\Omega)^n, \mathbf{v}^h \cdot \mathbf{n} = 0 \text{ on } \Gamma_1 \cup \Gamma_2 \cup \Gamma_c, \right. \\ &\quad \left. \mathbf{v}^h|_T \in \mathcal{P}^m(T), \forall T \in \mathcal{T}^h \text{ and } i \in \{1, 2\} \right\}, \end{aligned} \quad (27a)$$

$$Q_{\alpha_i}^h(\bar{\Omega}_i, \tilde{\mathcal{T}}_i^h) := \left\{ q_{\alpha_i}^h \in L_2(\bar{\Omega}_i) : q_{\alpha_i}^h = \alpha_i q^h, q^h \in L_2(\bar{\Omega}_i) \mid q^h|_T \in \mathcal{P}^{m-1}(T), \forall T \in \tilde{\mathcal{T}}_i^h \text{ and } i \in \{1, 2\} \right\}, \quad (27b)$$

where $\bar{\Omega}_i = \bar{\Omega}_i \cup \Omega_c$ and $\bar{\mathcal{T}}_i^h = \bar{\mathcal{T}}_i^h \cup \mathcal{T}_c^h$.

4.2. Discrete material representation

In addition to the material-dependent volume fractions (26), we introduce material-dependent densities ρ_i and specific internal energies e_i , discretized as smooth polynomials on each element. These variables allow to exactly represent a given discontinuity inside an element, which would be impossible with only a single density or energy. These fields are initialized in the following manner:

$$\rho_i(\mathbf{x}, t = 0) = \begin{cases} \rho_{0|i} & \alpha_i(\mathbf{x}, 0) > 0, \\ 0 & \alpha_i(\mathbf{x}, 0) = 0, \end{cases} \quad e_i(\mathbf{x}, t = 0) = \begin{cases} e_{0|i} & \alpha_i(\mathbf{x}, 0) > 0, \\ 0 & \alpha_i(\mathbf{x}, 0) = 0. \end{cases} \quad (28)$$

Here $\rho_{0|i}$ and $e_{0|i}$ provide additional values for material i in mixed elements, at points where the material's values are not defined by the initial conditions, i.e., $\rho_{0|i}$ and $e_{0|i}$ extend the initial conditions for material i wherever $\alpha_i(\mathbf{x}, t) > 0$. The time evolution of α_i in an element $T \in \mathcal{T}^h$ is computed by (26); this formula and $d\eta/dt = 0$ imply that changes in the volume fractions will occur due to local deformations of the mixed elements. While approaches based on closure models [15, 34] perform more complex operations to evolve volume fractions, in this work their evolution is based exclusively on the fluid velocity and we rely on the methods presented in Section 4.3 for the enforcement of interface conditions in the momentum and internal energy equations.

The evolution of material-specific densities ρ_i is governed by the principle of exact local mass conservation:

$$\rho_i(\mathbf{x}, t) = \frac{\rho_i(\mathbf{x}_0, 0)\alpha_i(\mathbf{x}_0, 0)}{J(\mathbf{x}, t)\alpha_i(\mathbf{x}, t)}, \quad (29)$$

where $\boldsymbol{\varphi}(\mathbf{x}_0, t) = \mathbf{x}$ and $\alpha_i(\mathbf{x}, t)\rho_i(\mathbf{x}, t)$ is the local mass of material i . Finally, the evolution of the specific internal energies e_i is governed by the weak forms of the internal energy equations as explained in Section 4.3.

4.3. A derivation of the weighted-shifted variational formulation

Let $\bar{\mathcal{E}}_1 = \bar{\Gamma}_1 \cup \mathcal{E}_c^o \cup \mathcal{E}_1^o$ and $\bar{\mathcal{E}}_2 = \bar{\Gamma}_2 \cup \mathcal{E}_c^o \cup \mathcal{E}_2^o$ be the unions of the edges/faces of the grid in two/three dimensions where the materials #1 and #2 are present, respectively, see Figure 4. That is to say, if an edge/face is in $\bar{\mathcal{E}}_i$, then material i is present at least on one of the sides of that edge/face (possibly both). For each side, the possibly discontinuous values of a field are indicated with the superscripts + and -, as shown in Figure 4. Across each side of the grid, the pressure p_1 of material #1 and p_2 of material #2 need to *separately* satisfy the following continuity conditions:

$$[p_1] = \mathbf{0}, \quad \text{on } \bar{\mathcal{E}}_1, \quad (30a)$$

$$[p_2] = \mathbf{0}, \quad \text{on } \bar{\mathcal{E}}_2, \quad (30b)$$

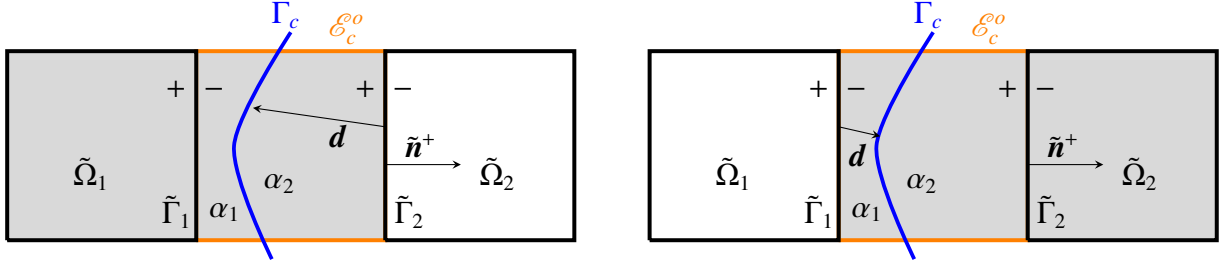
which will be enforced weakly, in what follows.

Next we introduce a definition of the jump of a field across an edge/face which is complementary to (4). For $i = 1$ or 2 , $[\zeta_i] = \zeta_i^+ \mathbf{n}^+ + \zeta_i^- \mathbf{n}^-$ for any scalar field ζ_i and $[\boldsymbol{\zeta}_i] = \boldsymbol{\zeta}_i^+ \cdot \mathbf{n}^+ + \boldsymbol{\zeta}_i^- \cdot \mathbf{n}^-$ for any vector field $\boldsymbol{\zeta}_i$. Observe that while (4) express jump conditions across a material interface, the previous definitions express a jump condition for a field associated with a single material across an edge/face of the grid. See again Figure 4.

To derive the weak form of the momentum equation, we start by considering material #1, as sketched in Case 1 of Figure 4a. Multiplying the strong form of the momentum equation by the test function $\boldsymbol{\psi}_{\alpha_1}^h \in \mathbf{V}_{\alpha_1}^h$ and integrating over the generic element T of the finite element mesh yields

$$(\rho_1 \dot{\mathbf{v}}, \alpha_1 \boldsymbol{\psi})_T - (p_1, \alpha_1 \nabla \cdot \boldsymbol{\psi})_T + (\mu_1 \nabla^s \mathbf{v}, \alpha_1 \nabla \boldsymbol{\psi})_T + \langle p_1, \alpha_1 \boldsymbol{\psi} \cdot \mathbf{n} \rangle_{\partial T} = 0. \quad (31)$$

The term $(\mu_1 \nabla^s \mathbf{v}, \alpha_1 \nabla \boldsymbol{\psi})_T$ contains the artificial viscosity tensor $\sigma_a = \mu_1 \nabla^s \mathbf{v}$: its complete definition can be found in [14]. Since the interface conditions (4) do not involve the artificial viscosity tensor, this term does not appear in any of the face integrals. This is equivalent to weakly enforce the continuity of the normal trace of the artificial



(a) Case 1: Treating the cut elements as part of material #1 weighted by α_1 .

(b) Case 2: Treating the cut elements as part of material #2 weighted by α_2 .

Figure 4: The two cases for treating the cut elements.

viscosity on each of the mesh faces. Summing over all the elements we have

$$\begin{aligned}
& (\rho_1 \dot{\mathbf{v}}, \alpha_1 \boldsymbol{\psi})_{\tilde{\Omega}_1} - (p_1, \alpha_1 \nabla \cdot \boldsymbol{\psi})_{\tilde{\Omega}_1} + (\mu_1 \alpha_1 \nabla^s \mathbf{v}, \nabla \boldsymbol{\psi})_{\tilde{\Omega}_1} \\
& + \langle [p_1], \{\alpha_1\}_{\alpha_1^-} \boldsymbol{\psi} \rangle_{\tilde{\Gamma}_1} + \langle \{p_1\}_{1-\alpha_1^-}, [\alpha_1] \boldsymbol{\psi} \rangle_{\tilde{\Gamma}_1} + \langle p_1^+, \alpha_1^+ \boldsymbol{\psi} \cdot \tilde{\mathbf{n}}^+ \rangle_{\tilde{\Gamma}_2} = 0,
\end{aligned} \tag{32}$$

where $\{\zeta\}_\gamma = \gamma \zeta^+ + (1 - \gamma) \zeta^-$ for $\gamma \in [0, 1]$ and any scalar or vector field ζ . Enforcing (30a) gives

$$\begin{aligned}
& (\rho_1 \dot{\mathbf{v}}, \alpha_1 \boldsymbol{\psi})_{\tilde{\Omega}_1} - (p_1, \alpha_1 \nabla \cdot \boldsymbol{\psi})_{\tilde{\Omega}_1} + (\mu_1 \alpha_1 \nabla^s \mathbf{v}, \nabla \boldsymbol{\psi})_{\tilde{\Omega}_1} \\
& + \langle \{p_1\}_{1-\alpha_1^-}, [\alpha_1] \boldsymbol{\psi} \rangle_{\tilde{\Gamma}_1 \cup \mathcal{E}_c^o} + \langle p_1^+, \alpha_1^+ \boldsymbol{\psi} \cdot \tilde{\mathbf{n}}^+ \rangle_{\tilde{\Gamma}_2} = 0.
\end{aligned} \tag{33}$$

Considering now material #2, as depicted in Case 2 of Figure 4b, we test the momentum equation with $\boldsymbol{\psi}_{\alpha_2}^h \in \mathbf{V}_{\alpha_2}^h$, and we follow analogous steps as above to enforce (30b):

$$(\rho_2 \dot{\mathbf{v}}, \alpha_2 \boldsymbol{\psi})_{\tilde{\Omega}_2} - (p_2, \alpha_2 \nabla \cdot \boldsymbol{\psi})_{\tilde{\Omega}_2} + (\mu_2 \alpha_2 \nabla^s \mathbf{v}, \nabla \boldsymbol{\psi})_{\tilde{\Omega}_2} + \langle \{p_2\}_{1-\alpha_2^+}, [\alpha_2] \boldsymbol{\psi} \rangle_{\tilde{\Gamma}_2 \cup \mathcal{E}_c^o} + \langle p_2^-, \alpha_2^- \boldsymbol{\psi} \cdot \tilde{\mathbf{n}}^- \rangle_{\tilde{\Gamma}_1} = 0. \tag{34}$$

Summing (33) and (34) and adding and subtracting $\langle \alpha_2^- p_1^-, \boldsymbol{\psi} \cdot \tilde{\mathbf{n}}^- \rangle_{\tilde{\Gamma}_1}$ and $\langle \alpha_1^+ p_2^+, \boldsymbol{\psi} \cdot \tilde{\mathbf{n}}^+ \rangle_{\tilde{\Gamma}_2}$ gives

$$\begin{aligned}
& (\rho_i \dot{\mathbf{v}}, \alpha_i \boldsymbol{\psi})_{\tilde{\Omega}} - (p_i, \alpha_i \nabla \cdot \boldsymbol{\psi})_{\tilde{\Omega}} + (\mu_i \alpha_i \nabla^s \mathbf{v}, \nabla \boldsymbol{\psi})_{\tilde{\Omega}} + \langle \llbracket p^- \rrbracket \cdot \mathbf{n}_1, \alpha_2^- \boldsymbol{\psi} \cdot \tilde{\mathbf{n}}^+ \rangle_{\tilde{\Gamma}_1} + \langle \llbracket p^+ \rrbracket \cdot \mathbf{n}_2, \alpha_1^+ \boldsymbol{\psi} \cdot \tilde{\mathbf{n}}^- \rangle_{\tilde{\Gamma}_2} \\
& + \langle \{p_1\}_{1-\alpha_1^-} [\alpha_1] + \{p_2\}_{1-\alpha_2^+} [\alpha_2], \boldsymbol{\psi} \rangle_{\mathcal{E}_c^o} = 0.
\end{aligned} \tag{35}$$

Enforcing the shifted conditions (19) on $\tilde{\Gamma}_1$ and $\tilde{\Gamma}_2$ yields

$$\begin{aligned}
& (\rho_i \dot{\mathbf{v}}, \alpha_i \boldsymbol{\psi})_{\tilde{\Omega}} - (p_i, \alpha_i \nabla \cdot \boldsymbol{\psi})_{\tilde{\Omega}} + (\mu_i \alpha_i \nabla^s \mathbf{v}, \nabla \boldsymbol{\psi})_{\tilde{\Omega}} \\
& - \langle \llbracket \sum_{k=1}^{m-1} \frac{\mathcal{D}_d^k p^-}{k!} \rrbracket \cdot \mathbf{n}_1, \alpha_2^- \boldsymbol{\psi} \cdot \tilde{\mathbf{n}}^+ \rangle_{\tilde{\Gamma}_1} - \langle \llbracket \sum_{k=1}^{m-1} \frac{\mathcal{D}_d^k p^+}{k!} \rrbracket \cdot \mathbf{n}_2, \alpha_1^+ \boldsymbol{\psi} \cdot \tilde{\mathbf{n}}^- \rangle_{\tilde{\Gamma}_2} \\
& + \langle \{p_1\}_{1-\alpha_1^-} [\alpha_1] + \{p_2\}_{1-\alpha_2^+} [\alpha_2], \boldsymbol{\psi} \rangle_{\mathcal{E}_c^o} = 0.
\end{aligned} \tag{36}$$

Noting that $[\alpha p] = \{\alpha\}_\gamma [p] + [\alpha] \{p\}_{1-\gamma}$ and $\alpha_2 = 1 - \alpha_1$, and recalling (30) and (19), we have

$$\begin{aligned}
& \{p_1\}_{1-\alpha_1^-} [\alpha_1] + \{p_2\}_{1-\alpha_2^+} [\alpha_2] = [\alpha_1 p_1 + \alpha_2 p_2] \\
& = (\alpha_1^+ p_1^+ - \alpha_1^- p_1^- + \alpha_2^+ p_2^+ - \alpha_2^- p_2^-) \tilde{\mathbf{n}}^+ \\
& = \left(\frac{(\alpha_1^+ - \alpha_1^-)}{2} p_1^+ + \frac{(\alpha_1^+ - \alpha_1^-)}{2} p_1^- - \frac{(\alpha_1^+ - \alpha_1^-)}{2} p_2^+ - \frac{(\alpha_1^+ - \alpha_1^-)}{2} p_2^- \right) \tilde{\mathbf{n}}^+ \\
& = \frac{\alpha_1^+ - \alpha_1^-}{2} (\llbracket p^- \rrbracket \cdot \mathbf{n}_1 + \llbracket p^+ \rrbracket \cdot \mathbf{n}_1) \tilde{\mathbf{n}}^+
\end{aligned}$$

$$= -\frac{\alpha_1^+ - \alpha_1^-}{2} \left(\left[\sum_{k=1}^{m-1} \frac{\mathcal{D}_d^k p^-}{k!} \right] \cdot \mathbf{n}_1 + \left[\sum_{k=1}^{m-1} \frac{\mathcal{D}_d^k p^+}{k!} \right] \cdot \mathbf{n}_1 \right) \tilde{\mathbf{n}}^+. \quad (37)$$

Substituting (37) into (36) yields the final two-material momentum equation with shifted interface conditions (note that we also added back the ignored volumetric viscosity terms):

$$\begin{aligned} & (\rho_i \dot{\mathbf{v}}, \alpha_i \boldsymbol{\psi})_\Omega - (p_i, \alpha_i \nabla \cdot \boldsymbol{\psi})_\Omega + (\mu_i \alpha_i \nabla^s \mathbf{v}, \nabla \boldsymbol{\psi})_\Omega \\ & - \left\langle \left[\sum_{k=1}^{m-1} \frac{\mathcal{D}_d^k p^-}{k!} \right] \cdot \mathbf{n}_1, \alpha_2^- \boldsymbol{\psi} \cdot \tilde{\mathbf{n}}^+ \right\rangle_{\tilde{\Gamma}_1} - \left\langle \left[\sum_{k=1}^{m-1} \frac{\mathcal{D}_d^k p^+}{k!} \right] \cdot \mathbf{n}_2, \alpha_1^+ \boldsymbol{\psi} \cdot \tilde{\mathbf{n}}^- \right\rangle_{\tilde{\Gamma}_2} \\ & - \left\langle \frac{\alpha_1^+ - \alpha_1^-}{2} \left(\left[\sum_{k=1}^{m-1} \frac{\mathcal{D}_d^k p^-}{k!} \right] \cdot \mathbf{n}_1 + \left[\sum_{k=1}^{m-1} \frac{\mathcal{D}_d^k p^+}{k!} \right] \cdot \mathbf{n}_1 \right), \boldsymbol{\psi} \cdot \tilde{\mathbf{n}}^+ \right\rangle_{\mathcal{E}_c^o} = 0. \end{aligned} \quad (38)$$

To derive the weak form of the internal energy equation, we follow the typical steps of a local discontinuous Galerkin (LDG) formulation. Starting with material #1 and multiplying the strong form of the internal equation by the test function $\phi_{\alpha_1}^h \in Q_{\alpha_1}^h$ and over a generic element $T \in \bar{\Omega}_1$ yields

$$(\rho_1 \dot{e}_1, \alpha_1 \phi)_T - (\mathbf{v}, \nabla(\alpha_1 \phi p_1))_T + \langle \mathbf{v} \cdot \mathbf{n}, \alpha_1 \phi p_1 \rangle_{\partial T} - (\mu_1 \alpha_1 \nabla^s \mathbf{v}, \nabla \mathbf{v})_T = 0. \quad (39)$$

Replacing the boundary velocity trace, \mathbf{v} , by a *numerical flux*, $\hat{\mathbf{v}}$, yields

$$(\rho_1 \dot{e}_1, \alpha_1 \phi)_T - (\mathbf{v}, \nabla(\alpha_1 \phi p_1))_T + \langle \hat{\mathbf{v}} \cdot \mathbf{n}, \alpha_1 \phi p_1 \rangle_{\partial T} - (\mu_1 \alpha_1 \nabla^s \mathbf{v}, \nabla \mathbf{v})_T = 0. \quad (40)$$

The numerical flux $\hat{\mathbf{v}}$ accomplishes the linking of the numerical solution between neighboring elements, and will be defined momentarily. Summing over all the elements and integrating back by parts we have

$$\begin{aligned} & (\rho_1 \dot{e}_1, \alpha_1 \phi)_{\bar{\Omega}_1} + (p_1 \nabla \cdot \mathbf{v}, \alpha_1 \phi)_{\bar{\Omega}_1} - (\mu_1 \alpha_1 \nabla^s \mathbf{v}, \nabla \mathbf{v})_{\bar{\Omega}_1} \\ & + \langle \llbracket \hat{\mathbf{v}} \rrbracket \cdot \tilde{\mathbf{n}}^+, \{\alpha_1 \phi p_1\}_{\gamma_1} \rangle_{\tilde{\Gamma}_1 \cup \tilde{\Gamma}_2 \cup \mathcal{E}_c^o} + \langle \{\hat{\mathbf{v}}\}_{1-\gamma_1}, [\alpha_1 \phi p_1] \rangle_{\tilde{\Gamma}_1 \cup \tilde{\Gamma}_2 \cup \mathcal{E}_c^o} \\ & - \langle \llbracket \mathbf{v} \rrbracket \cdot \tilde{\mathbf{n}}^+, \{\alpha_1 \phi p_1\}_{\gamma_1} \rangle_{\tilde{\Gamma}_1 \cup \tilde{\Gamma}_2 \cup \mathcal{E}_c^o} - \langle \{\mathbf{v}\}_{1-\gamma_1}, [\alpha_1 \phi p_1] \rangle_{\tilde{\Gamma}_1 \cup \tilde{\Gamma}_2 \cup \mathcal{E}_c^o} = 0. \end{aligned} \quad (41)$$

We define the normal and tangential components of $\hat{\mathbf{v}}$ as

$$\llbracket \hat{\mathbf{v}} \rrbracket \cdot \mathbf{n}_1 = - \left[\sum_{k=1}^m \frac{\mathcal{D}_d^k \mathbf{v}}{k!} \right] \cdot \mathbf{n}_1, \quad \llbracket \hat{\mathbf{v}} \rrbracket \cdot \boldsymbol{\tau}_1^i = \llbracket \mathbf{v} \rrbracket \cdot \boldsymbol{\tau}_1^i, \quad (42)$$

where $\boldsymbol{\tau}_1^i$ is a unit tangent vector to the true interface (repeated index notation is implied). The normal component of the numerical flux, $\llbracket \hat{\mathbf{v}} \rrbracket \cdot \mathbf{n}_1$, mimics (22) while $\llbracket \hat{\mathbf{v}} \rrbracket \cdot \boldsymbol{\tau}_1^i$ is the same as the body-fitted case. Noting that the relation $\llbracket \hat{\mathbf{v}} \rrbracket = (\llbracket \hat{\mathbf{v}} \rrbracket \cdot \mathbf{n}_1) \mathbf{n}_1 + (\llbracket \hat{\mathbf{v}} \rrbracket \cdot \boldsymbol{\tau}_1^i) \boldsymbol{\tau}_1^i$, holds for any vector $\hat{\mathbf{v}}$, the interface conditions for \mathbf{v} can be reflected by setting

$$\llbracket \hat{\mathbf{v}} \rrbracket = - \left(\left[\sum_{k=1}^m \frac{\mathcal{D}_d^k \mathbf{v}}{k!} \right] \cdot \mathbf{n}_1 \right) \mathbf{n}_1 + (\llbracket \mathbf{v} \rrbracket \cdot \boldsymbol{\tau}_1^i) \boldsymbol{\tau}_1^i, \quad \{\{\hat{\mathbf{v}}\}\}_{1-\gamma} = \{\{\mathbf{v}\}\}_{1-\gamma}, \quad (43)$$

where the choice for $\{\{\hat{\mathbf{v}}\}\}_{1-\gamma}$ is exactly the same as that for the body-fitted. Once the above substitutions are made, and using the fact that $\llbracket \mathbf{v} \rrbracket = 0$ on internal faces as the velocity space \mathcal{V} is continuous, the discrete variational form reads

$$(\rho_1 \dot{e}_1, \alpha_1 \phi)_{\bar{\Omega}_1} + (p_1 \nabla \cdot \mathbf{v}, \alpha_1 \phi)_{\bar{\Omega}_1} - (\mu_1 \alpha_1 \nabla^s \mathbf{v}, \nabla \mathbf{v})_{\bar{\Omega}_1} - \langle \llbracket \mathbf{S}_h^m \mathbf{v} \rrbracket \cdot \mathbf{n}_1 (\tilde{\mathbf{n}}^+ \cdot \mathbf{n}_1), \{\alpha_1 \phi p_1\}_{\gamma_1} \rangle_{\tilde{\Gamma}_1 \cup \tilde{\Gamma}_2 \cup \mathcal{E}_c^o} = 0. \quad (44)$$

Finally, to improve stability, we add a diffusion-type double jump terms at the surrogate interfaces to obtain the

final internal energy variational form for material #1:

$$\begin{aligned}
& (\rho_1 \dot{e}_1, \alpha_1 \phi)_{\tilde{\Omega}_1} + (p_1 \nabla \cdot \mathbf{v}, \alpha_1 \phi)_{\tilde{\Omega}_1} - (\mu_1 \alpha_1 \nabla^s \mathbf{v}, \nabla \mathbf{v})_{\tilde{\Omega}_1} - \langle \llbracket \mathbf{S}_h^m \mathbf{v} \rrbracket \cdot \mathbf{n}_1 (\tilde{\mathbf{n}}^+ \cdot \mathbf{n}_1), \{\alpha_1 \phi p_1\}_{\gamma_1} \rangle_{\tilde{\Gamma}_1 \cup \tilde{\Gamma}_2 \cup \mathcal{E}_e^o} \\
& + \langle (1 - \alpha_1) \{d |\nabla \mathbf{v}|\}_{\gamma} \left(p_1^+ - p_2^- + \sum_{k=1}^{m-1} \frac{\mathcal{D}_d^k (p_1^+ - p_2^-)}{k!} \right), [S_h^{m-1} \phi] \cdot \tilde{\mathbf{n}}^+ \rangle_{\tilde{\Gamma}_1} \\
& + \langle \alpha_1 \{d |\nabla \mathbf{v}|\}_{\gamma} \left(p_1^+ - p_2^- + \sum_{k=1}^{m-1} \frac{\mathcal{D}_d^k (p_1^+ - p_2^-)}{k!} \right), [S_h^{m-1} \phi] \cdot \tilde{\mathbf{n}}^+ \rangle_{\tilde{\Gamma}_2} = 0.
\end{aligned} \tag{45}$$

Note that the diffusion terms in (45) are shifted, i.e., they represent the pressure jump at the true interface. Similarly, to derive the weak form of the internal energy equation for material #2, we follow the same procedure as for material #1, but this time we multiply the strong form of the internal equation by the test function $\phi_{\alpha_2}^h \in \mathcal{Q}_{\alpha_2}^h$. Thus, the final internal energy variational form for material #2 reads

$$\begin{aligned}
& (\rho_2 \dot{e}_2, \alpha_2 \phi)_{\tilde{\Omega}_2} + (p_2 \nabla \cdot \mathbf{v}, \alpha_2 \phi)_{\tilde{\Omega}_2} - (\mu_2 \alpha_2 \nabla^s \mathbf{v}, \nabla \mathbf{v})_{\tilde{\Omega}_2} - \langle \llbracket \mathbf{S}_h^m \mathbf{v} \rrbracket \cdot \mathbf{n}_1 (\tilde{\mathbf{n}}^+ \cdot \mathbf{n}_1), \{\alpha_2 \phi p_2\}_{\gamma_2} \rangle_{\tilde{\Gamma}_1 \cup \tilde{\Gamma}_2 \cup \mathcal{E}_e^o} \\
& + \langle \alpha_2 \{d |\nabla \mathbf{v}|\}_{\gamma} \left(p_1^+ - p_2^- + \sum_{k=1}^{m-1} \frac{\mathcal{D}_d^k (p_1^+ - p_2^-)}{k!} \right), [S_h^{m-1} \phi] \cdot \tilde{\mathbf{n}}^+ \rangle_{\tilde{\Gamma}_1} \\
& + \langle (1 - \alpha_2) \{d |\nabla \mathbf{v}|\}_{\gamma} \left(p_1^+ - p_2^- + \sum_{k=1}^{m-1} \frac{\mathcal{D}_d^k (p_1^+ - p_2^-)}{k!} \right), [S_h^{m-1} \phi] \cdot \tilde{\mathbf{n}}^+ \rangle_{\tilde{\Gamma}_2} = 0.
\end{aligned} \tag{46}$$

The conservation properties of the above formulation are discussed in Appendix A.

Remark 2. Note that the mass matrices in (38), (45), and (46) remain constant in time due to (29).

5. Numerical Results

All simulations are performed in a customized version of the open-source Laghos proxy application [22], which is based on the MFEM finite element library [2].

5.1. Smooth two-dimensional Taylor-Green Vortex

The purpose of this example is to confirm that the method can retain high-order convergence for a smooth problem. The example can be seen as a patch-like test where a smooth single-material simulation is altered by adding an artificial interface between two identical materials.

The domain is $[0, 1] \times [0, 1]$ with $\mathbf{v} \cdot \mathbf{n} = 0$ (slip) boundary conditions. For all tests, a vertical interface is initially positioned at $x = 0.5 + \Delta x$. The initial velocity, densities and pressures are set as:

$$\mathbf{v} = \{\sin(\pi x) \cos(\pi y), -\cos(\pi x) \sin(\pi y)\}, \quad \rho_i = 1, \quad p_i = \frac{\rho_i}{4} (\cos(2\pi x) + \cos(2\pi y)), \quad \gamma_i = \frac{5}{3},$$

where the material-specific quantities are initialized only on their side of the interface, and in the cut elements. The right-hand sides of the specific internal energy equations include the following source terms:

$$e_{i,src} = \frac{3\pi}{8} \alpha_i (\cos(3\pi x) \cos(\pi y) - \cos(\pi x) \cos(3\pi y)).$$

This setup guarantees that the velocity, material energies, and densities do not change in time, i.e. $\partial/\partial t = 0$, but they do vary along particle trajectories, i.e., $d/dt \neq 0$, which allows to compare to the exact solution at any time; see Section 8.1 in [14] for more details. Figure 5 shows an example results for a $Q_3 - Q_2$ simulation with 2 mesh refinements (8×8 elements). As our shifted face terms contain jumps in ∇p at the surrogate interfaces, the numerical discretization of p_k introduces additional errors. This test demonstrates that these errors converge with the expected rate as we increase the polynomial order and take higher Taylor expansions of p_k .

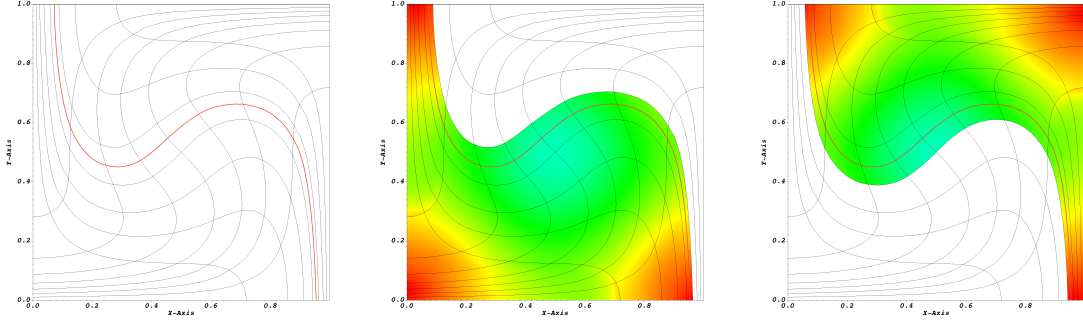


Figure 5: Final mesh and interface position (left), and specific internal energies (middle and right) at $t = 0.75$ for a $Q_3 - Q_2$ discretization of the two-dimensional Taylor Green vortex.

For all simulations we use reconstruct 4th order pressure functions and take 4 Taylor expansion terms in the shifted integrals. The distances to the interface are recomputed at every time by the normalization-based distance solver. We test convergence for $Q_2 - Q_1$, $Q_3 - Q_2$, and $Q_4 - Q_3$ discretizations, which should produce 2nd, 3rd, and 4th order, respectively. Table 1 shows the L1 velocity errors there we observe the expected convergence rates. Figure 6 shows the convergence plot corresponding to Table 1, and convergence plots of the total momentum and total energy errors, which also converge as expected.

ref	Q2Q1 L1 error	rate	Q3Q2 L1 error	rate	Q4Q3 L1 error	rate
0	7.93E-2	-	2.68E-2	-	3.85E-2	-
1	4.67E-2	0.76	7.15E-3	1.91	3.08E-3	3.64
2	7.50E-3	2.64	7.32E-4	3.29	2.30E-4	3.74
3	1.44E-3	2.38	9.01E-5	3.02	9.84E-6	4.55
4	2.61E-4	2.46	1.13E-5	2.99	3.91E-7	4.65

Table 1: Convergence tests for the two-dimensional Taylor Green problem.

5.2. Two-material one-dimensional Sod shock tube

Next we consider a two-material Riemann problem in one dimension. This problem tests the Shifted Interface Method's ability to equilibrate a pressure discontinuity, and allows to compare the behavior of the method to case of a fitted interface.

The domain is $[0, 1]$ with $v(0) = v(1) = 0$ boundary conditions. Both materials are ideal gases with equation of state $p = (\gamma - 1)\rho e$. The interface is at $x_c = 0.5$ for the fitted simulations and is moved to $x_c = 0.5 + 0.5\Delta x$ for the shifted interface simulations. The problem is run to a final time of $t = 0.2$. The two initial states are:

$$(v, \rho, e, p, \gamma) = \begin{cases} (0, 1, 2, 2, 2) & \text{if } x < x_c \text{ (Left material),} \\ (0, 0.125, 2, 0.1, 1.4) & \text{if } x > x_c \text{ (Right material).} \end{cases}$$

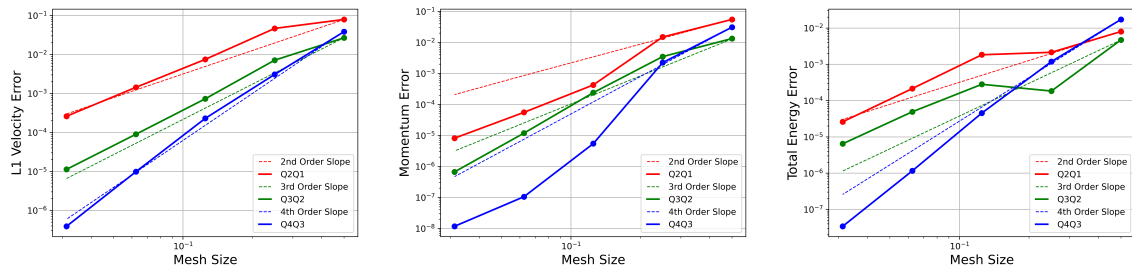


Figure 6: Convergence plots: L1 velocity errors, momentum errors, and total energy errors for the two-dimensional Taylor Green problem.

The problem is run on 100 elements with a $Q_2 - Q_1$ discretization. To stress the effects of the shifted face integrals, we compare two sets of results, namely, (i) the results obtained with the presented method, and (ii) results obtained by the same simulation without including the shifted face integrals. Results from case (i) are in Figure 7, showing the final material pressures, their evolution in time at the interface, and the time evolution of the material volume fractions. Visualized point values (e.g., on the left panel of Figure 7) correspond to the quadrature points that are used to compute all volumetric integrals (4 points per element in this case). For each material, a quantity is visualized at a given point x whenever $\eta_0(x_0) \geq 0$, where x_0 is the initial position of x . We observe that the pressures equilibrate similarly to the fitted case, while the volume of the left material expands in the mixed element, as expected. The corresponding results of case (ii) are in Figure 8. We observe that the pressures do not equilibrate, and the materials do not expand (left material) and compress (right material) correctly. The final velocity, material densities, and material internal energies for case (i) are shown in Figure 9. Although the pressures are in equilibrium, oscillations in the material densities and specific internal energies are present in the mixed element. This is a known issue for Lagrangian methods that do not add artificial diffusion around the contact discontinuity. Note that the shifted interface terms are also unable to detect such oscillations, as the terms use information only about the gradients of pressure and velocity, which are zero at the equilibrated contact.

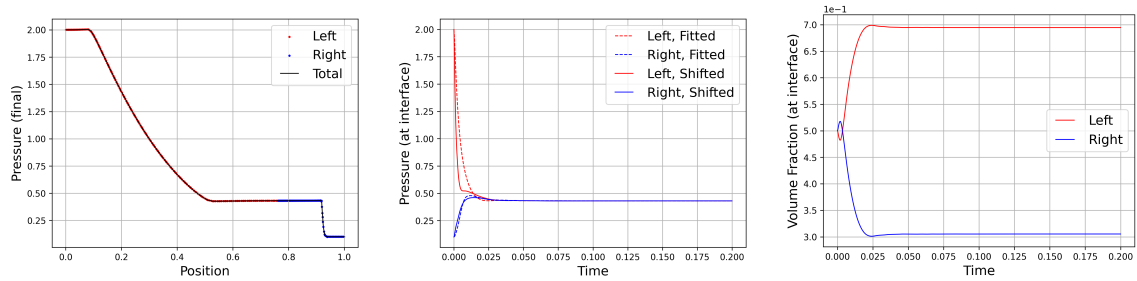


Figure 7: Simulation with *active* shifted interface terms: final material pressures (left), pressures' time-history at the interface (middle), volume fractions' time-history at the interface (right), for the one-dimensional Sod tube test.

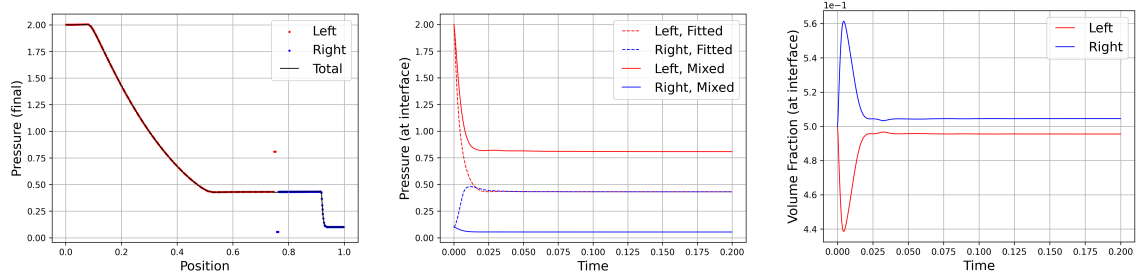


Figure 8: Simulation with *inactive* shifted interface terms: final material pressures (left), pressures' time-history at the interface (middle), volume fractions' time-history at the interface (right), for the one-dimensional Sod tube test.

5.3. 1D Water-Air Shock Tube

The next test is a more severe one dimensional Riemann problem. It represents a water-air interaction with a large initial pressure jump. This problem tests the robustness of the Shifted Interface Method under extreme conditions.

The domain is $[0, 1]$ with $v(0) = v(1) = 0$ boundary conditions. The high-pressure water (left side) material is represented by the stiffened gas equation of state $p = (\gamma - 1)\rho e - \gamma 6 \times 10^8$. The low-pressure air (right side) material represented by ideal gas with equation of state $p = (\gamma - 1)\rho e$. The interface is at $x_c = 0.7$ for the fitted

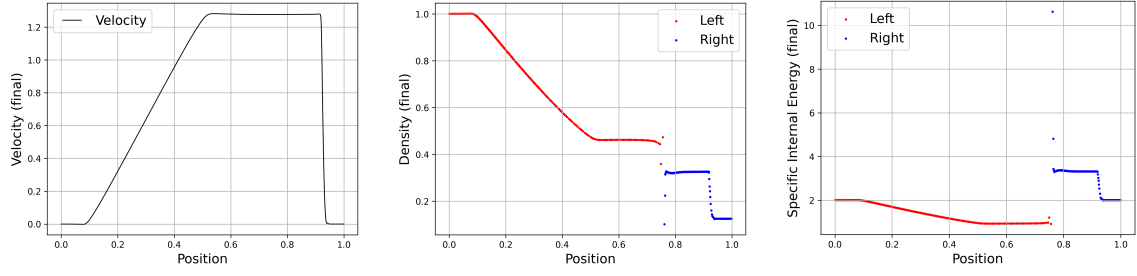


Figure 9: Final velocity, material densities, and material specific internal energies for the one-dimensional Sod tube test.

simulations and is moved to $x_c = 0.7 + 0.5\Delta x$ for the shifted interface simulations. The two initial states are:

$$(v, \rho, p, \gamma) = \begin{cases} (0, 10^3, 10^9, 4.4) & \text{if } x < x_c \text{ (Left material),} \\ (0, 50, 10^5, 1.4) & \text{if } x > x_c \text{ (Right material).} \end{cases}$$

The problem is run on 200 elements with a $Q_2 - Q_1$ discretization. Again we compare (i) the results obtained with the presented method, and (ii) results obtained by the same simulation without including the shifted face integrals. Results from case (i) are in Figure 10, showing the final material pressures, their evolution in time at the interface, and the time evolution of the material volume fractions (Section 5.2 explains the visualization of the point values). The corresponding results of case (ii) are in Figure 11. We make similar observations as in the Sod test, namely, the shifted terms are able to equilibrate the material pressures, and expand the left material near the interface. The final velocity, material densities, and material internal energies for case (i) are shown in Figure 12. Again we observe some oscillations of the material-specific densities and specific internal energies around the cut element, due to the lack of artificial viscosity around the contact region. The more concerning behavior, however, occurs at the end of the rarefaction region of the left material, where the final pressure is negative and the corresponding velocity has a pronounced oscillation. We do not fully understand this behavior and we are exploring ways to improve it.

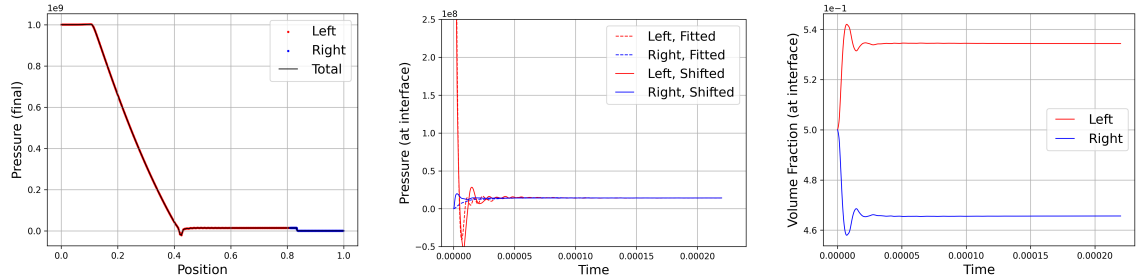


Figure 10: Simulation with *active* shifted interface terms: final material pressures (left), pressures' time-history at the interface (middle), volume fractions' time-history at the interface (right), for the one-dimensional Water-Air shock tube test.

5.4. Two-dimensional and three-dimensional Triple Point Interaction.

This example demonstrates the main advantage of the method, namely, the ability to maintain sharp curved material interfaces inside curved zones for complex two-dimensional and three-dimensional problems. The test is a modification of the standard Triple Point problem from [14], Section 8.5.

The domain is $x \in [0, 7] \times y \in [0, 3]$ in two dimensions, and $x \in [0, 7] \times y \in [0, 3] \times z \in [0, 3]$ in three dimensions with $\mathbf{v} \cdot \mathbf{n} = 0$ boundary conditions. At $t = 0$ we set a non-fitted material interface as shown in the left panels of Figures 13 and Figures 14. We denote the left/top material with #1, while the bottom/right region is

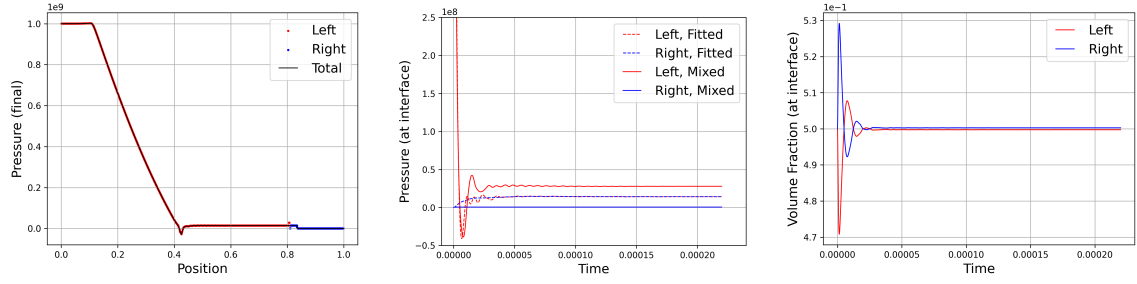


Figure 11: Simulation with *inactive* shifted interface terms: final material pressures (left), pressures' time-history at the interface (middle), volume fractions' time-history at the interface (right), for the one-dimensional Water-Air shock tube test.

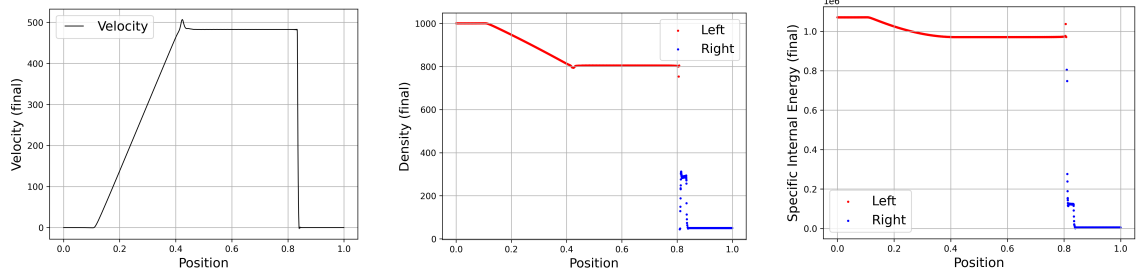


Figure 12: Final velocity, material densities, and material specific internal energies for the Water-Air shock tube test.

occupied by material #2. The three initial states are (where $z = 0$ in the two-dimensional setup):

$$(v, \rho, p, \gamma) = \begin{cases} (0, 1, 1, 1.5) & \text{for Material \#1, } x < 1, \\ (0, 0.125, 0.1, 1.5) & \text{for Material \#1, } x > 1, z < 1.5, \\ (0, 1, 0.1, 1.5) & \text{for Material \#1, } x > 1, z > 1.5, \\ (0, 1, 0.1, 1.4) & \text{for Material \#2, } z < 1.5, \\ (0, 0.125, 0.1, 1.4) & \text{for Material \#2, } z > 1.5. \end{cases}$$

Although the jumps in material properties are not large, the resulting material interfaces are rather complex. Density plots for both materials at times $t = 2.5$ and $t = 5$ are shown in Figures 13 and 14 for the two- and three-dimensional simulations, respectively. We observe that the Shifted Interface Method is able to produce reasonable results in both two and three dimensions, while maintaining the sharp interface representation, as designed in the method's construction. This test is also a good example of the method's generality with respect to dimension, as it is based on finite elements and does not involve explicit geometric operations.

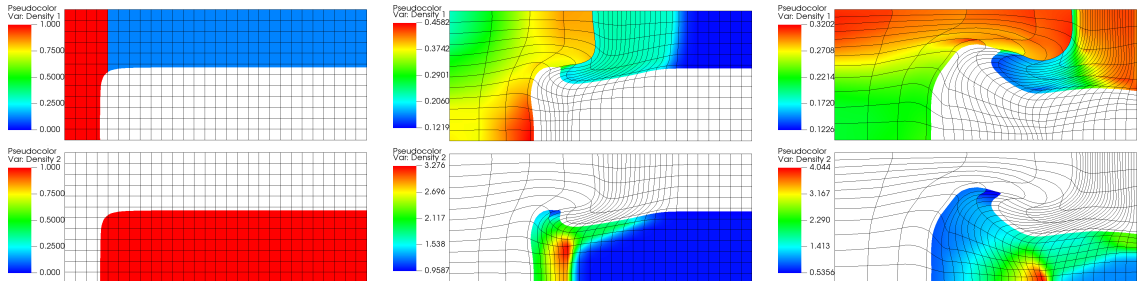


Figure 13: Material densities (#1 on top, #2 on bottom) at times $t = 0$, $t = 2.5$, and $t = 5$ for the two-dimensional Triple Point interaction problem.

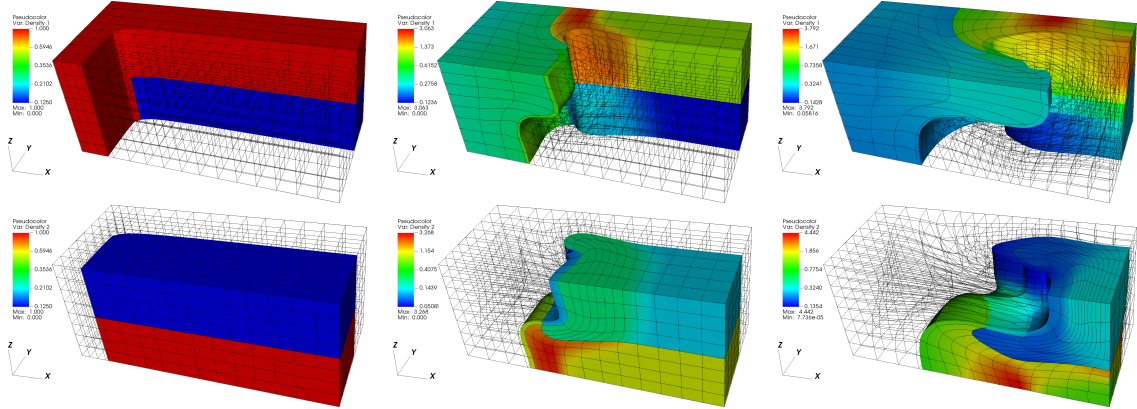


Figure 14: Material densities (#1 on top, #2 on bottom) at times $t = 0$, $t = 2.5$, and $t = 5$ for the three-dimensional Triple Point interaction problem.

6. Conclusions

We proposed the WSIM, a high-order, two-material Lagrangian shock hydrodynamics algorithm. The proposed approach utilizes the exact location of the material interface to evolve the system, while maintaining a continuous curved interface compatible with curvilinear grids. The interface evolution does not involve any geometric operations and is general with respect to dimension, mesh curvature, and FE discretization order. We demonstrated that WSIM is capable of (i) representing evolving interfaces to the order of accuracy of the underlying high-order discretization spaces, (ii) equilibrating pressure values for challenging 1D benchmark problems, and (iii) maintaining sharp material interfaces inside curved elements for complex two- and three-dimensional shock problems. For these reasons, WSIM can represent a new pathway in the (sharp) representation of moving interfaces.

Our future efforts will concentrate on expanding into the Arbitrary Lagrangian-Eulerian framework. This extension holds the most promise, particularly in eliminating diffusion within the material interface regions by remapping the level set function. Additionally, our plans include extending the methodology to accommodate an arbitrary number of materials. Furthermore, we intend to combine the WSIM with the Shifted Boundary Method to weakly enforce wall boundary conditions in complex geometries.

Acknowledgments

The authors of Duke University are gratefully thanking the generous support of Lawrence Livermore National Laboratories, through a Laboratory Directed Research & Development (LDRD) Agreement. This work performed under the auspices of the U.S. Department of Energy by Lawrence Livermore National Laboratory under Contract DE-AC52-07NA27344, LLNL-JRNL-854557. Guglielmo Scovazzi has also been partially supported by the National Science Foundation, Division of Mathematical Sciences (DMS), under Grant 2207164.

Appendix A. Conservation properties

To start the discussion, let us consider a body-fitted variational formulation that corresponds to the limit case of the WSIM when $\mathbf{d} \rightarrow \mathbf{0}$, so that $\tilde{\Gamma} \rightarrow \Gamma_I$, $\tilde{\mathbf{n}} \rightarrow \mathbf{n}$, $\tilde{\mathbf{n}} \cdot \mathbf{n} = 1$ and $\tilde{\mathbf{n}} \cdot \boldsymbol{\tau}_i = 0$. In this limit, (38), (45), and (46) reduce to:

$$(\boldsymbol{\psi}, \rho \dot{\mathbf{v}})_\Omega - (\nabla \cdot \boldsymbol{\psi}, p)_\Omega + (\mu \nabla^s \mathbf{v}, \nabla \boldsymbol{\psi})_\Omega = 0, \quad (\text{A.1a})$$

$$(\phi, \rho \dot{e})_\Omega + (\phi, p \nabla \cdot \mathbf{v})_\Omega - (\mu \nabla^s \mathbf{v}, \nabla \mathbf{v})_\Omega = 0. \quad (\text{A.1b})$$

Let us assume, as is customary when proving conservation statements, that only homogenous Neumann (zero-traction) boundary conditions are imposed. Setting $\boldsymbol{\psi} = \mathbf{e}_i$ (where \mathbf{e}_i is the unit vector along the i th coordinate axis):

$$\partial_t(1, \rho \mathbf{v} \cdot \mathbf{e}_i)_\Omega = 0, \quad i = 1 \dots d, \quad (\text{A.2a})$$

which states that global integral of the momentum is conserved over time for the semi-discrete system of equations. The global statement of conservation of total energy is obtained setting $\phi = 1$ in the energy equation, $\boldsymbol{\psi} = \mathbf{v}$ in the momentum equation (to obtain a kinetic energy balance), and summing the results:

$$\partial_t(1, \rho(\mathbf{v} \cdot \mathbf{v}/2 + e))_\Omega = (\nabla \cdot \mathbf{v}, p)_\Omega - (1, p \nabla \cdot \mathbf{v})_\Omega = 0. \quad (\text{A.3})$$

The conservation of momentum statement for the WSIM is achieved analogously to the body-fitted variational form. Namely, setting $\boldsymbol{\psi} = \mathbf{e}_j$ in (38) yields

$$\begin{aligned} & (\rho_1, \dot{\mathbf{v}} \cdot \mathbf{e}_j)_{\tilde{\Omega}_1^h} + (\rho_2, \dot{\mathbf{v}} \cdot \mathbf{e}_j)_{\tilde{\Omega}_2^h} + (\rho_i \alpha_i, \dot{\mathbf{v}} \cdot \mathbf{e}_j)_{\Omega_c} = \\ & \langle \llbracket \sum_{k=1}^{m-1} \frac{\mathcal{D}_d^k p^-}{k!} \rrbracket \cdot \mathbf{n}_1, \alpha_2^- \mathbf{e}_j \cdot \tilde{\mathbf{n}}^+ \rangle_{\tilde{\Gamma}_1} + \langle \llbracket \sum_{k=1}^{m-1} \frac{\mathcal{D}_d^k p^+}{k!} \rrbracket \cdot \mathbf{n}_2, \alpha_1^+ \mathbf{e}_j \cdot \tilde{\mathbf{n}}^- \rangle_{\tilde{\Gamma}_2} \\ & + \langle \frac{\alpha_1^+ - \alpha_1^-}{2} \left(\llbracket \sum_{k=1}^{m-1} \frac{\mathcal{D}_d^k p^-}{k!} \rrbracket \cdot \mathbf{n}_1 + \llbracket \sum_{k=1}^{m-1} \frac{\mathcal{D}_d^k p^+}{k!} \rrbracket \cdot \mathbf{n}_1 \right), \mathbf{e}_j \cdot \tilde{\mathbf{n}}^+ \rangle_{\mathcal{E}_c^o}, \end{aligned} \quad (\text{A.4a})$$

Adding $\langle \llbracket p^- \rrbracket \cdot \mathbf{n}_1, \alpha_2^- \mathbf{e}_j \cdot \tilde{\mathbf{n}}^+ \rangle_{\tilde{\Gamma}_1} + \langle \llbracket p^+ \rrbracket \cdot \mathbf{n}_2, \alpha_1^+ \mathbf{e}_j \cdot \tilde{\mathbf{n}}^- \rangle_{\tilde{\Gamma}_2} + \langle \frac{\alpha_1^+ - \alpha_1^-}{2} (\llbracket p^- \rrbracket + \llbracket p^+ \rrbracket) \cdot \mathbf{n}_1, \mathbf{e}_j \cdot \tilde{\mathbf{n}}^+ \rangle_{\mathcal{E}_c^o}$ to both sides of (A.4a) yields,

$$\begin{aligned} & (\rho_1, \dot{\mathbf{v}} \cdot \mathbf{e}_j)_{\tilde{\Omega}_1^h} + (\rho_2, \dot{\mathbf{v}} \cdot \mathbf{e}_j)_{\tilde{\Omega}_2^h} + (\rho_i \alpha_i, \dot{\mathbf{v}} \cdot \mathbf{e}_j)_{\Omega_c} + \langle \llbracket p^- \rrbracket \cdot \mathbf{n}_1, \alpha_2^- \mathbf{e}_j \cdot \tilde{\mathbf{n}}^+ \rangle_{\tilde{\Gamma}_1} \\ & + \langle \llbracket p^+ \rrbracket \cdot \mathbf{n}_2, \alpha_1^+ \mathbf{e}_j \cdot \tilde{\mathbf{n}}^- \rangle_{\tilde{\Gamma}_2} + \langle \frac{\alpha_1^+ - \alpha_1^-}{2} (\llbracket p^- \rrbracket + \llbracket p^+ \rrbracket) \cdot \mathbf{n}_1, \mathbf{e}_j \cdot \tilde{\mathbf{n}}^+ \rangle_{\mathcal{E}_c^o} = e_{mom}(\mathbf{e}_j), \end{aligned} \quad (\text{A.4b})$$

where

$$\begin{aligned} e_{mom}(\mathbf{e}_j) & = \langle \llbracket S_h^{m-1} p^- \rrbracket \cdot \mathbf{n}_1, \alpha_2^- \mathbf{e}_j \cdot \tilde{\mathbf{n}}^+ \rangle_{\tilde{\Gamma}_1} + \langle \llbracket S_h^{m-1} p^+ \rrbracket \cdot \mathbf{n}_2, \alpha_1^+ \mathbf{e}_j \cdot \tilde{\mathbf{n}}^- \rangle_{\tilde{\Gamma}_2} \\ & + \langle \frac{\alpha_1^+ - \alpha_1^-}{2} \llbracket S_h^{m-1} (p^- + p^+) \rrbracket \cdot \mathbf{n}_1, \mathbf{e}_j \cdot \tilde{\mathbf{n}}^+ \rangle_{\mathcal{E}_c^o}. \end{aligned} \quad (\text{A.4c})$$

The face terms in the left-hand side of (A.5d) represent the fluxes entering and exiting $\tilde{\Omega}_1^h, \tilde{\Omega}_2^h$ and Ω_c , respectively, due to pressure jump between material #1 and #2. Therefore the left-hand side of (A.5d) represents the momentum balance in the whole domain. The presence of the material pressure jump terms across \mathcal{E}_c^o is due to the fact that the material pressures are not restricted to just $\tilde{\Omega}_1^h$ and $\tilde{\Omega}_2^h$, but are extended to Ω_c . Finally, from [4], $e_{mom} \rightarrow 0$ in the asymptotic limit at a rate of $O(h^m)$. In other words, the formulation admits a momentum error that is caused by the Taylor expansion approximation; this error converges to zero with the order of the Taylor expansion.

A statement of global total energy conservation can be achieved summing the energy equation, tested with $\phi = 1$, and the momentum equation, tested with $\boldsymbol{\psi} = \mathbf{v}$:

$$\begin{aligned} & \partial_t(1, \rho_1(\mathbf{v} \cdot \mathbf{v}/2 + e_1))_{\tilde{\Omega}_1^h} + \partial_t(1, \rho_2(\mathbf{v} \cdot \mathbf{v}/2 + e_2))_{\tilde{\Omega}_2^h} + \partial_t(1, \alpha_1 \rho_1(\mathbf{v} \cdot \mathbf{v}/2 + e_1))_{\Omega_c} \\ & + \partial_t(1, \alpha_2 \rho_2(\mathbf{v} \cdot \mathbf{v}/2 + e_2))_{\Omega_c} = \langle \llbracket S_h^m \mathbf{v} \rrbracket \cdot \mathbf{n}_1 (\tilde{\mathbf{n}}^+ \cdot \mathbf{n}_1), \{\alpha_1 p_1\}_{\gamma_1} + \{\alpha_2 p_2\}_{\gamma_2} \rangle_{\tilde{\Gamma}_1 \cup \tilde{\Gamma}_2 \cup \mathcal{E}_c^o} \\ & + \langle \llbracket \sum_{k=1}^{m-1} \frac{\mathcal{D}_d^k p^-}{k!} \rrbracket \cdot \mathbf{n}_1, \alpha_2^- \mathbf{v} \cdot \tilde{\mathbf{n}}^+ \rangle_{\tilde{\Gamma}_1} + \langle \llbracket \sum_{k=1}^{m-1} \frac{\mathcal{D}_d^k p^+}{k!} \rrbracket \cdot \mathbf{n}_2, \alpha_1^+ \mathbf{v} \cdot \tilde{\mathbf{n}}^- \rangle_{\tilde{\Gamma}_2} \\ & + \langle \frac{\alpha_1^+ - \alpha_1^-}{2} \left(\llbracket \sum_{k=1}^{m-1} \frac{\mathcal{D}_d^k p^-}{k!} \rrbracket \cdot \mathbf{n}_1 + \llbracket \sum_{k=1}^{m-1} \frac{\mathcal{D}_d^k p^+}{k!} \rrbracket \cdot \mathbf{n}_1 \right), \mathbf{v} \cdot \tilde{\mathbf{n}}^+ \rangle_{\mathcal{E}_c^o}, \end{aligned} \quad (\text{A.5a})$$

Adding $\langle \llbracket p^- \rrbracket \cdot \mathbf{n}_1, \alpha_2^- \mathbf{v} \cdot \tilde{\mathbf{n}}^+ \rangle_{\tilde{\Gamma}_1} + \langle \llbracket p^+ \rrbracket \cdot \mathbf{n}_2, \alpha_1^+ \mathbf{v} \cdot \tilde{\mathbf{n}}^- \rangle_{\tilde{\Gamma}_2} + \langle \frac{\alpha_1^+ - \alpha_1^-}{2} (\llbracket p^- \rrbracket + \llbracket p^+ \rrbracket) \cdot \mathbf{n}_1, \mathbf{v} \cdot \tilde{\mathbf{n}}^+ \rangle_{\mathcal{E}_c^o}$ to both sides of (A.5a) yields,

$$\begin{aligned} & \partial_t(1, \rho_1(\mathbf{v} \cdot \mathbf{v}/2 + e_1))_{\tilde{\Omega}_1^h} + \partial_t(1, \rho_2(\mathbf{v} \cdot \mathbf{v}/2 + e_2))_{\tilde{\Omega}_2^h} + \partial_t(1, \alpha_1 \rho_1(\mathbf{v} \cdot \mathbf{v}/2 + e_1))_{\Omega_c} \\ & + \partial_t(1, \alpha_2 \rho_2(\mathbf{v} \cdot \mathbf{v}/2 + e_2))_{\Omega_c} + \langle \llbracket p^- \rrbracket \cdot \mathbf{n}_1, \alpha_2^- \mathbf{v} \cdot \tilde{\mathbf{n}}^+ \rangle_{\tilde{\Gamma}_1} + \langle \llbracket p^+ \rrbracket \cdot \mathbf{n}_2, \alpha_1^+ \mathbf{v} \cdot \tilde{\mathbf{n}}^- \rangle_{\tilde{\Gamma}_2} \\ & + \langle \frac{\alpha_1^+ - \alpha_1^-}{2} (\llbracket p^- \rrbracket + \llbracket p^+ \rrbracket) \cdot \mathbf{n}_1, \mathbf{v} \cdot \tilde{\mathbf{n}}^+ \rangle_{\mathcal{E}_c^o} \\ & = \langle \llbracket \mathbf{S}_h^m \mathbf{v} \rrbracket \cdot \mathbf{n}_1(\tilde{\mathbf{n}}^+ \cdot \mathbf{n}_1), \{\alpha_1 p_1\}_{\gamma_1} + \{\alpha_2 p_2\}_{\gamma_2} \rangle_{\tilde{\Gamma}_1 \cup \tilde{\Gamma}_2 \cup \mathcal{E}_c^o} + e_{mom}(\mathbf{v}). \end{aligned} \quad (\text{A.5b})$$

Similarly to the momentum derivation, the left-hand side of (A.5b) represents the total energy balance in the whole domain. In the asymptotic limit, from [4], $\llbracket \mathbf{S}_h^m \mathbf{v} \rrbracket \cdot \mathbf{n}_1 \rightarrow 0$ at a rate of $O(h^{m+1})$ and $e_{mom} \rightarrow 0$ at a rate of $O(h^m)$. Therefore the formulation admits a total energy error that goes to zero with the order of the Taylor expansion.

The form of the momentum (A.4b) and the total energy (A.5b) statements are not traditional. A different way to interpret these statements is to use the Gauss divergence theorem on $(\alpha_i \nabla p_i, \mathbf{e}_j)_{\Omega_c}$. Applying (30a)- (30b) and following the same steps as Section 4.3 yields

$$\begin{aligned} (\alpha_i \nabla p_i, \mathbf{e}_j)_{\Omega_c} & = \langle \llbracket p^- \rrbracket \cdot \mathbf{n}_1, \alpha_2^- \mathbf{e}_j \cdot \tilde{\mathbf{n}}^+ \rangle_{\tilde{\Gamma}_1} + \langle p_1^-, \mathbf{e}_j \cdot \tilde{\mathbf{n}}^- \rangle_{\tilde{\Gamma}_1} \\ & + \langle \llbracket p^+ \rrbracket \cdot \mathbf{n}_2, \alpha_1^+ \mathbf{e}_j \cdot \tilde{\mathbf{n}}^- \rangle_{\tilde{\Gamma}_2} + \langle p_2^+, \mathbf{e}_j \cdot \tilde{\mathbf{n}}^+ \rangle_{\tilde{\Gamma}_2} + \langle \frac{\alpha_1^+ - \alpha_1^-}{2} (\llbracket p^- \rrbracket + \llbracket p^+ \rrbracket) \cdot \mathbf{n}_1, \mathbf{e}_j \cdot \tilde{\mathbf{n}}^+ \rangle_{\mathcal{E}_c^o} \end{aligned} \quad (\text{A.5c})$$

Thus, plugging (A.5c) in (A.4b) yields

$$(\rho_1, \dot{\mathbf{v}} \cdot \mathbf{e}_j)_{\tilde{\Omega}_1^h} + (\rho_2, \dot{\mathbf{v}} \cdot \mathbf{e}_j)_{\tilde{\Omega}_2^h} - \langle p_1^-, \mathbf{e}_j \cdot \tilde{\mathbf{n}}^- \rangle_{\tilde{\Gamma}_1} - \langle p_2^+, \mathbf{e}_j \cdot \tilde{\mathbf{n}}^+ \rangle_{\tilde{\Gamma}_2} = e_{mom}(\mathbf{e}_j) - \underbrace{(\rho_i \dot{\mathbf{v}} + \nabla p_i, \alpha_i \mathbf{e}_j)_{\Omega_c}}_{O(h^m)}, \quad (\text{A.5d})$$

where

$$\begin{aligned} e_{mom}(\mathbf{e}_j) & = \langle \llbracket \mathbf{S}_h^{m-1} p^- \rrbracket \cdot \mathbf{n}_1, \alpha_2^- \mathbf{e}_j \cdot \tilde{\mathbf{n}}^+ \rangle_{\tilde{\Gamma}_1} + \langle \llbracket \mathbf{S}_h^{m-1} p^+ \rrbracket \cdot \mathbf{n}_2, \alpha_1^+ \mathbf{e}_j \cdot \tilde{\mathbf{n}}^- \rangle_{\tilde{\Gamma}_2} \\ & + \langle \frac{\alpha_1^+ - \alpha_1^-}{2} \llbracket \mathbf{S}_h^{m-1} (p^- + p^+) \rrbracket \cdot \mathbf{n}_1, \mathbf{e}_j \cdot \tilde{\mathbf{n}}^+ \rangle_{\mathcal{E}_c^o} \\ & = O(h^m). \end{aligned} \quad (\text{A.5e})$$

In regards to the statement of global total energy conservation (A.5b), we first rewrite it as

$$\begin{aligned} & \partial_t(1, \rho(\mathbf{v} \cdot \mathbf{v}/2 + e_1))_{\tilde{\Omega}_1^h} + \partial_t(1, \rho(\mathbf{v} \cdot \mathbf{v}/2 + e_2))_{\tilde{\Omega}_2^h} = -(\rho_1 \dot{e}_1 + p_1 \nabla \cdot \mathbf{v}, \alpha_1)_{\Omega_c} - (\rho_2 \dot{e}_2 + p_2 \nabla \cdot \mathbf{v}, \alpha_2)_{\Omega_c} \\ & + \langle \llbracket \mathbf{S}_h^m \mathbf{v} \rrbracket \cdot \mathbf{n}_1(\tilde{\mathbf{n}}^+ \cdot \mathbf{n}_1), \{\alpha_1 p_1\}_{\gamma_1} + \{\alpha_2 p_2\}_{\gamma_2} \rangle_{\tilde{\Gamma}_1 \cup \tilde{\Gamma}_2 \cup \mathcal{E}_c^o} \\ & - (\alpha_i \rho_i, \dot{\mathbf{v}} \cdot \mathbf{v})_{\Omega_c} + (\alpha_i p_i, \nabla \cdot \mathbf{v})_{\Omega_c} \\ & + \langle \llbracket \sum_{k=1}^{m-1} \frac{\mathcal{D}_d^k p^-}{k!} \rrbracket \cdot \mathbf{n}_1, \alpha_2^- \mathbf{v} \cdot \tilde{\mathbf{n}}^+ \rangle_{\tilde{\Gamma}_1} + \langle \llbracket \sum_{k=1}^{m-1} \frac{\mathcal{D}_d^k p^+}{k!} \rrbracket \cdot \mathbf{n}_2, \alpha_1^+ \mathbf{v} \cdot \tilde{\mathbf{n}}^- \rangle_{\tilde{\Gamma}_2} \\ & + \langle \frac{\alpha_1^+ - \alpha_1^-}{2} \left(\llbracket \sum_{k=1}^{m-1} \frac{\mathcal{D}_d^k p^-}{k!} \rrbracket \cdot \mathbf{n}_1 + \llbracket \sum_{k=1}^{m-1} \frac{\mathcal{D}_d^k p^+}{k!} \rrbracket \cdot \mathbf{n}_1 \right), \mathbf{v} \cdot \tilde{\mathbf{n}}^+ \rangle_{\mathcal{E}_c^o}, \end{aligned} \quad (\text{A.5f})$$

The first three terms on the right-hand side approach 0 at a rate of $O(h^{m+1})$. At this point, we employ Gauss divergence theorem for $(\alpha_i p_i, \nabla \cdot \mathbf{v})_{\Omega_c}$, recall (30a)- (30b) and follow the same steps as Section 4.3, yielding

$$\begin{aligned} & \partial_t(1, \rho_1(\mathbf{v} \cdot \mathbf{v}/2 + e_1))_{\tilde{\Omega}_1^h} + \partial_t(1, \rho_2(\mathbf{v} \cdot \mathbf{v}/2 + e_2))_{\tilde{\Omega}_2^h} - \langle p_1^-, \mathbf{v} \cdot \tilde{\mathbf{n}}^- \rangle_{\tilde{\Gamma}_1} - \langle p_2^+, \mathbf{v} \cdot \tilde{\mathbf{n}}^+ \rangle_{\tilde{\Gamma}_2} = \\ & O(h^{m+1}) - \underbrace{(\rho_i \dot{\mathbf{v}} + \nabla p_i, \alpha_i \mathbf{v})_{\Omega_c}}_{O(h^m)} + e_{mom}(\mathbf{v}) = O(h^m). \end{aligned} \quad (\text{A.5g})$$

References

- [1] Rémi Abgrall, Konstantin Lipnikov, Nathaniel Morgan, and Svetlana Tokareva. Multidimensional staggered grid residual distribution scheme for Lagrangian hydrodynamics. *SIAM J. Sci. Comp.*, 42(1):A343–A370, 2020.
- [2] Robert Anderson, Julian Andrej, Andrew Barker, Jamie Bramwell, Jean-Sylvain Camier, Jakub Cerveny, Veselin A. Dobrev, Yohann Dudouit, Aaron Fisher, Tzanio V. Kolev, Will Pazner, Mark Stowell, Vladimir Z. Tomov, Ido Akkerman, Johann Dahm, David Medina, and Stefano Zampini. MFEM: a modular finite elements methods library. *Comput. Math. Appl.*, 81:42–74, 2021.
- [3] Robert W. Anderson, Veselin A. Dobrev, Tzanio V. Kolev, Robert N. Rieben, and Vladimir Z. Tomov. High-order multi-material ALE hydrodynamics. *SIAM J. Sci. Comp.*, 40(1):B32–B58, 2018.
- [4] Nabil M. Atallah, Claudio Canuto, and Guglielmo Scovazzi. Analysis of the shifted boundary method for the Poisson problem in general domains. *Mathematics of Computation*, 2020. Submitted.
- [5] Nabil M Atallah, Claudio Canuto, and Guglielmo Scovazzi. The high-order shifted boundary method and its analysis. *Computer Methods in Applied Mechanics and Engineering*, 394:114885, 2022.
- [6] A. Barlow, R. Hill, and M. J. Shashkov. Constrained optimization framework for interface-aware sub-scale dynamics closure model for multimaterial cells in Lagrangian and arbitrary Lagrangian-Eulerian hydrodynamics. *J. Comput. Phys.*, 276(0):92–135, 2014.
- [7] Andrew J. Barlow, Pierre-Henri Maire, William J. Rider, Robert N. Rieben, and Mikhail J. Shashkov. Arbitrary Lagrangian-Eulerian methods for modeling high-speed compressible multimaterial flows. *J. Comput. Phys.*, 322:603–665, 2016.
- [8] Christopher Basting and Dmitri Kuzmin. A minimization-based finite element formulation for interface-preserving level set reinitialization. *Computing*, 95:13–25, 2013.
- [9] Alexander G. Belyaev and Pierre-Alain Fayolle. On variational and PDE-based distance function approximations. *Comput. Graphics Forum*, 34(8):104–118, 2015.
- [10] David J. Benson. Computational methods in Lagrangian and Eulerian hydrocodes. *Comput. Methods Appl. Mech. Eng.*, 99:235–394, 1992.
- [11] Walter Boscheri and Michael Dumbser. High order accurate direct arbitrary-Lagrangian-Eulerian ADER-WENO finite volume schemes on moving curvilinear unstructured meshes. *Comput. Fluids*, 136:48–66, 2016.
- [12] Oriol Colomé, Alex Main, Léo Nouveau, and Guglielmo Scovazzi. A weighted Shifted Boundary Method for free surface flow problems. *Journal of Computational Physics*, 424:109837, 2021.
- [13] B. Després and F. Lagoutière. Numerical resolution of a two-component compressible fluid model with interfaces. *Progress in Computational Fluid Dynamics, an International Journal*, 7(6):295–310, 2007.
- [14] V. Dobrev, Tz. Kolev, and R. Rieben. High-order curvilinear finite element methods for Lagrangian hydrodynamics. *SIAM J. Sci. Comp.*, 34(5):606–641, 2012.
- [15] Veselin. A. Dobrev, Tzanio. V. Kolev, Robert. N. Rieben, and Vladimir Z. Tomov. Multi-material closure model for high-order finite element Lagrangian hydrodynamics. *Int. J. Numer. Methods Fluids*, 82(10):689–706, 2016.
- [16] Elena Gaburro, Walter Boscheri, Simone Chiocchetti, Christian Klingenberg, Volker Springel, and Michael Dumbser. High order direct Arbitrary-Lagrangian-Eulerian schemes on moving Voronoi meshes with topology changes. *J. Comput. Phys.*, 407:109167, 2020.
- [17] Jean-Luc Guermond, Bojan Popov, and Vladimir Z. Tomov. Entropy-viscosity method for the single material Euler equations in Lagrangian frame. *Comput. Methods Appl. Mech. Eng.*, 300:402–426, 2016.
- [18] C. W. Hirt, A. A. Amsden, and J. L. Cook. An arbitrary Lagrangian-Eulerian computing method for all flow speeds. *J. Comput. Phys.*, 14:277–253, 1974.
- [19] J. R. Kamm and M. J. Shashkov. A pressure relaxation closure model for one-dimensional, two-material Lagrangian hydrodynamics based on Riemann problem. *Commun. Comput. Phys.*, 7(5):927–976, 2010.
- [20] J. R. Kamm, M. J. Shashkov, J. Fung, A. K. Harrison, and T. R. Canfield. A comparative study of various pressure relaxation closure models for one-dimensional two-material Lagrangian hydrodynamics. *Int J. Num. Meth. Fluids*, 65:1311–1324, 2011.
- [21] Tzanio V. Kolev, Paul Fischer, Misun Min, Jack Dongarra, Jed Brown, Veselin Dobrev, Timothy Warburton, Stanimire Tomov, Mark Shephard, Ahmad Abdelfattah, Valeria Barra, Natalie Beams, Jean-Sylvain Camier, Noel Chalmers, Yohann Dudouit, Ali Karakus, Ian Karlin, Stefan Kerkemeier, Yu-Hsiang Lan, David Medina, Elia Merzari, Aleksandr Obabko, Will Pazner, Thilina Rathnayake, Cameron Smith, Lukas Spies, Kasia Świrydowicz, Jeremy Thompson, Ananias Tomboulides, and Vladimir Z. Tomov. Efficient exascale discretizations: High-order finite element methods. *Int. J. High Perform. Comput. Appl.*, 2021.
- [22] Laghos: High-order Lagrangian hydrodynamics miniapp, 2019. <http://github.com/CEED/Laghos>.
- [23] Kangan Li, Nabil M. Atallah, Alex G. Main, and Guglielmo Scovazzi. The shifted interface method: A flexible approach to embedded interface computations. *Int. J. Numer. Methods Eng.*, 121(3):492–518, 2020.
- [24] Xiaodong Liu, Nathaniel R. Morgan, and Donald E. Burton. A high-order Lagrangian discontinuous Galerkin hydrodynamic method for quadratic cells using a subcell mesh stabilization scheme. *J. Comput. Phys.*, 386:110–157, 2019.
- [25] R. Loubere, J. Ovadia, and R. Abgrall. A Lagrangian discontinuous Galerkin-type method on unstructured meshes to solve hydrodynamics problems. *Int J. Num. Meth. Fluids*, 44:645–663, 2004.
- [26] A. Main and G. Scovazzi. The shifted boundary method for embedded domain computations. Part I: Poisson and Stokes problems. *Journal of Computational Physics*, 372:972–995, 2018.
- [27] A. Main and G. Scovazzi. The shifted boundary method for embedded domain computations. Part II: Linear advection–diffusion and incompressible Navier-Stokes equations. *Journal of Computational Physics*, 372:996–1026, 2018.
- [28] P-H. Maire. A high-order cell-centered Lagrangian scheme for two-dimensional compressible fluid flows on unstructured meshes. *J. Comput. Phys.*, 228(7):2931–2425, 2009.
- [29] P-H. Maire, J. Breil, and S. Galera. A cell-centred arbitrary Lagrangian-Eulerian (ALE) method. *Int J. Num. Meth. Fluids*, 56:1161–1166, 2004.
- [30] D. Miller and G. Zimmerman. An algorithm for time evolving volume fractions in mixed zones in Lagrangian hydrodynamics calculations. *Russian J. of Phys. Chem. B, Focus on Physics*, 3(1):117–121, 2009.

- [31] B. Müller, F. Kummer, and M. Oberlack. Highly accurate surface and volume integration on implicit domains by means of moment-fitting. *Int. J. Numer. Methods Eng.*, 96(8):512–528, 2013.
- [32] J. Von Neumann and R.D. Richtmyer. A method for the numerical calculation of hydrodynamic shocks. *J. Appl. Phys.*, 21, 1950.
- [33] A. López Ortega and G. Scovazzi. A geometrically-conservative, synchronized, flux-corrected remap for arbitrary Lagrangian-Eulerian computations with nodal finite elements. *J. Comp. Phys.*, 230(17):6709–6741, July 2011.
- [34] Aditya K. Pandare, Jacob Waltz, and Jozsef Bakosi. Multi-material hydrodynamics with algebraic sharp interface capturing. *Comput. Fluids*, 215:104804, 2021.
- [35] Aditya K. Pandare, Jacob Waltz, Weizhao Li, Hong Luo, and Jozsef Bakosi. On the design of stable, consistent, and conservative high-order methods for multi-material hydrodynamics. *J. Comput. Phys.*, 490:112313, 2023.
- [36] Manuel Quezada de Luna, Dmitri Kuzmin, and Christopher E. Kees. A monolithic conservative level set method with built-in redistancing. *J. Comput. Phys.*, 379:262–278, 2019.
- [37] V. L. Rvachev. *Theory of R-functions and Some Applications (In Russian)*. Nauk Dumka, 1982.
- [38] G. Scovazzi. Lagrangian shock hydrodynamics on tetrahedral meshes: A stable and accurate variational multiscale approach. *J. Comp. Phys.*, 231(24):8029–8069, December 2012.
- [39] G. Scovazzi, M. Christon, T. Hughes, and J. Shadid. Stabilized shock hydrodynamics: I. a Lagrangian method. *Comp. Methods in Applied Mech. Eng.*, 196:923–966, 2007.
- [40] Guglielmo Scovazzi, Edward Love, and MJ Shashkov. Multi-scale lagrangian shock hydrodynamics on q1/p0 finite elements: Theoretical framework and two-dimensional computations. *Computer methods in applied mechanics and engineering*, 197(9-12):1056–1079, 2008.
- [41] Mikhail Shashkov. An adaptive moments-based interface reconstruction using intersection of the cell with one half-plane, two half-planes and a circle. *J. Comput. Phys.*, page 112504, 2023.
- [42] Mikhail Shashkov and Eugene Kikinon. Moments-based interface reconstruction, remap and advection. *J. Comput. Phys.*, 479:111998, 2023.
- [43] T. Song, A. Main, G. Scovazzi, and M. Ricchiuto. The shifted boundary method for hyperbolic systems: Embedded domain computations of linear waves and shallow water flows. *Journal of Computational Physics*, 369:45–79, 2018.
- [44] Mark Sussman, Peter Smereka, and Stanley Osher. A level set approach for computing solutions to incompressible two-phase flow. *J. Comput. Phys.*, 114(1):146–159, 1994.
- [45] Arturo Vargas, Thomas M. Stitt, Kenneth Weiss, Vladimir Z. Tomov, Jean-Sylvain Camier, Tzanio Kolev, and Robert N. Rieben. Matrix-free approaches for GPU acceleration of a high-order finite element hydrodynamics application using MFEM, Umpire, and RAJA. *Int. J. High Perform. Comput. Appl.*, 36(4):492–509, 2022.
- [46] J. Waltz, N.R. Morgan, T.R. Canfield, M.R.J. Charest, L.D. Risinger, and J.G. Wohlbiel. A three-dimensional finite element arbitrary Lagrangian-Eulerian method for shock hydrodynamics on unstructured grids. *Comput. Fluids*, 92:172–187, 2014.
- [47] Feng Xiao, Satoshi Ii, and Chungang Chen. Revisit to the THINC scheme: A simple algebraic VOF algorithm. *J. Comput. Phys.*, 230(19):7086–7092, 2011.
- [48] Y. Yanilkin, E. Goncharov, V. Kolobyanin, V. Sadchikov, J. R. Kamm, M. J. Shashkov, and W. J. Rider. Multi-material pressure relaxation methods for Lagrangian hydrodynamics. *Comput. Fluids*, 83:137–143, 2013.
- [49] David Youngs. Time-dependent multi-material flow with large fluid distortion. *Num. Method Fluid Dyn.*, 24:273–285, 1982.